Schweizerische Eidgenossenschaft
Confédération suisse
Confederazione Svizzera
Confederaziun svizra

Final report dated 30-03-2020

Fracture Design for Geothermal Reservoir (EDGAR)

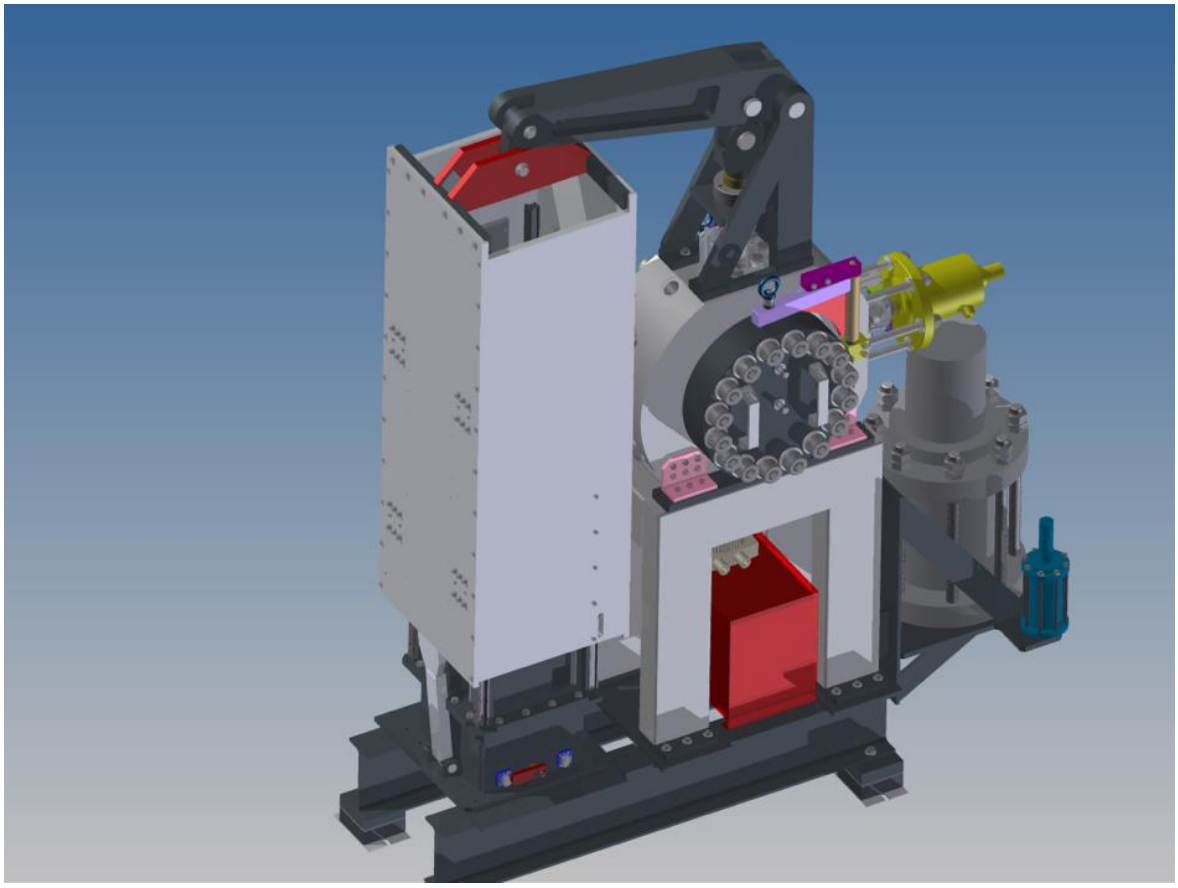

Source: Schematic diagram of the triaxial cell “HighSTEPS”, which was built by the company RMP Srl

Date: 30.03.2020

Location: Lausanne

Publisher:
Office fédéral de l'énergie OFEN
Section Recherche énergétique et cleantech
CH-3003 Berne
www.bfe.admin.ch

Subsidy recipients:
EPFL
Laboratoire expérimental de mécanique des roches
GC D1 401
Station 18
1015 Lausanne
www.epfl.ch

ETHZ
Sonneggstrasse 5
8092 Zürich
www.ethz.ch

Geo-Energie Suisse AG
Reitergasse 11
8004 Zürich
www.geo-energie.ch

Authors:
Chiara Cornelio, EPFL, chiara.cornelio@epfl.ch
Marie Violay, EPFL, marie.violay@epfl.ch
Carolina Giorgetti, EPFL, carolina.giorgetti@epfl.ch

SFOE project coordinators:
Men Wirz, men.wirz@bfe.admin.ch
Céline Weber, cweber@focus-e.ch

SFOE contract number: SI/501495-01

The authors bear the entire responsibility for the content of this report and for the conclusions drawn therefrom.

Abstract

Engineered geothermal systems (EGS) projects have attempted to apply hydraulic, acid and thermal stimulations to improve the transmissivity between wells and create a network of fractures that allows for sustainable extraction of heat stored in the solid rock matrix. So far, the stimulation procedures have not been fully designed, and consequently induced seismicity is still a risk. Within this project, we investigate the role of fluid and in particular fluid viscosity in the context of induced seismicity due to geothermal reservoir stimulation. In particular, we developed a new experimental apparatus able to reproduce geothermal in situ conditions. Moreover, we performed several series of experiments to address the role of fluid viscosity in the entire seismic cycle (i.e. earthquakes reactivation, earthquakes nucleation and earthquakes propagation). The fluid viscosity property showed an ambiguous behavior in our experimental results: the increase of fluid viscosity trapped on the slip surface promotes the earthquake nucleation, but under some condition of slip velocity and fault roughness, it increases the energy necessary for earthquakes propagation.

The complexity of the analyzed problem and the uncertainties of state of stresses, geometry and lithologies of the fractures in real geothermal systems do not allow us to establish universal and general rules for the injection of viscous fluids in field operations.

However, the results of this project answer fundamental questions about the role of viscous fluids on faults and fractures behavior. Further research, especially in pilot project for fluid injection at intermediate scale, can build on and benefit from the presented results. In particular, the results of this pilot project showed that also the rheology of the used fluids in the field operation can have an impact on the seismic risk linked to stimulation and production phases of geo-reservoirs.

Résumé

Les projets de géothermie profonde de type EGS utilisent des stimulations hydrauliques, chimiques et thermiques pour améliorer la transmissivité entre les puits et créer un réseau de fractures permettant l'extraction durable de la chaleur stockée dans la matrice rocheuse. Ces stimulations peuvent augmenter le risque potentiel de sismicité induite. Dans le cadre de ce projet, nous étudions le rôle de la viscosité du fluide d'injection sur la mécanique des failles au long du cycle séismique (c'est-à-dire de la réactivation des failles, la nucléation à propagation des tremblements de terre). En particulier, nous avons développé un nouvel appareil expérimental capable de reproduire les conditions des réservoirs géothermiques. Plusieurs séries d'expériences ont montré que la viscosité du fluide a un comportement ambigu : l'augmentation de la viscosité du fluide piégé sur la surface de glissement favorise la nucléation du séisme, mais sous certaines conditions de vitesse de glissement et de rugosité de la faille, elle augmente l'énergie nécessaire à la propagation des tremblements de terre.

La complexité du problème analysé et les incertitudes liées à l'état des contraintes *in-situ*, la géométrie et les lithologies des fractures dans les systèmes géothermiques réels ne permettent pas d'établir des règles universelles et générales pour l'injection de fluides visqueux dans les opérations de terrain.

Cependant, les résultats de ce projet répondent à des questions fondamentales concernant le rôle des fluides visqueux sur le comportement des failles et des fractures. Des recherches supplémentaires, en particulier dans le cadre d'un projet pilote d'injection de fluide à échelle intermédiaire, peuvent s'appuyer sur les résultats présentés et en tirer parti. En particulier, les résultats de ce projet pilote ont montré que la rhéologie des fluides utilisés sur le terrain peut avoir un impact sur le risque sismique lié aux phases de stimulation et de production des géo-réservoirs.

Contents

1 Introduction and background

A natural geothermal system is defined by three key factors:

1. High geothermal gradients (hot rock at relatively shallow depth);
2. Water to transport the heat from the rocks; and
3. Well-developed fracture and pore networks as surface area for heat exchange of fluid percolating through the rocks.

If one of the last three elements is missing, the conditions for the energy supply are not ideal and the system needs to be stimulated.

Reservoir stimulations consist of high pressure injection of stimulation fluid into a wellbore to create new cracks or to reactivate already existing micro-cracks, first in the vicinity of the wellbore and secondly in the geothermal reservoir. The dominant physical parameters that control fracturing and fracture reactivation can be subdivided into 6 main categories:

1. Initial fracture geometry;
2. Fluid leak-off rate;
3. Fluid rheology (i.e. low/high fluid viscosity);
4. Rock mass properties around the fracture;
5. Chemistry of additives to the stimulation fluid;
6. Stress state.

Engineered Geothermal System (EGS) projects have attempted to apply hydraulic, acid and thermal stimulations to improve the transmissivity between wells and create a network of fractures that allows for sustainable extraction of heat stored in the solid rock matrix. So far, this has not been fully designed using engineering principles, partially because hydraulic stimulation models only assume mode I (opening) fracture. Indeed, chemical and/or hydraulic stimulations in EGS may induce micro-seismic events (mode II or III or shearing fractures in a sliding mode) due to reactivation of pre-existing fractures and faults. Unstable events leading to a seismic response in geothermal reservoirs originate from different mechanisms; the most important are:

1. Pore-pressure increase which acts against normal stress and reduces the normal effective stress;
2. Change in local stress conditions due to fluid volume change;
3. Temperature decrease: cold fluids injection can cause fracture contraction (reduces contact area) and therefore static friction;
4. Chemical alteration of fracture surfaces.

Fracture, friction and fault geometry are the key parameters controlling earthquake mechanics (Ohnaka, 2003). Faults respond to fluid-induced stress perturbations depending on their stability state by (stage I) remaining locked, by (stage II) undergoing slow and stable sliding, by (stage III) experiencing local on-fault short-lived unstable events (earthquake precursory sequence), or by (stage IV) accelerating towards

catastrophic seismic slip (main event) (Kaneko, et al., 2010). Therefore, the velocities involved in a seismic cycle can cover 10 order of magnitude, from 10^{-9} ms^{-1} to 10^{1} ms^{-1} (Figure 1).

- During stage I and at low slip velocity (10^{-9}-10^{-4} $m \cdot s^{-1}$, i.e. fault reactivation), the linear Mohr-Coulomb failure criterion is often used to describe the initial condition of a fault. The change in stress configuration of a fault due to injection of a fluid consists of an increase of the pore pressure (P_p) and of a decrease of the effective normal stress $P_{eff} = \sigma - P_p$, where σ is the normal stress. In a shear stress vs. normal stress plot, this consists in shifting the Mohr circle to the left side of the plot.

- Transition from stage I to stage II, III or IV, i.e. earthquake nucleation, is described, for example by the *rate- and state- friction theory* (Dieterich, 1979; Ruina, 1983), where frictional stability depends on three main frictional parameters: the instantaneous velocity (a), a variable of state (b) and the critical distance D_c. The critical distance represents, for a given velocity, the slip distance necessary to regenerate new asperities at the contact surface. At steady state conditions, if the combined parameter $(a - b) = \frac{\partial \mu_{ss}}{\partial [\ln(V)]} < 0$, where $\partial \mu_{ss}$ is the variation in steady-state friction upon a variation in velocity ∂V, the friction is rate-weakening and sliding can be stable or unstable. If $a > b$, friction is rate-strengthening and only stable sliding is possible because the rupture propagation is difficult.

- Stage 4 corresponds to earthquake rupture propagation and co-seismic slip velocities (up to 10 m/s). In the past 15 years, the installation and exploitation of rotary shear apparatus designed to achieve the large slip rates (i.e, > 1cm/s) typical of earthquakes rupture propagation and displacements produced unexpected experimental results. Among these, the most surprising is the dramatic drop in friction (of up to 90% in most cases) at seismic slip rates, independent of the rock type. Up to date, very few high velocity friction experiments have been performed with pore fluid pressure (Violay, et al., 2013; Violay, et al., 2014; Violay, et al., 2015). Moreover, these studies do not consider the properties of the fluids. To explain the strong frictional fault weakening in presence of fluid observed at high velocity many different weakening mechanisms have been proposed:

1. Thermal pressurization (Sibson, 1973): pore pressure increases due to frictional heating;

2. Flash heating (Rice, 2006): the temperature rises during frictional slip can reduce the strength of contacting asperities. The degradation of a large amount of asperities involves an overall reduction of the mean friction coefficient.

3. Elasto-hydrodynamic (EHD) lubrication (Brodsky & Kanamori, 2001): a layer of viscous fluid can lubricate the entire fault surface, decreasing the strength of the interface. The presence of a highly viscous fluid in natural faults can be due to man-made injection activities or to the presence of a rock melt produced by the temperature increase during seismic slip. The elasto-hydrodynamic theory recognizes three different lubrication regimes: I) boundary lubrication regime (BL) II) mixed lubrication regime and III) fully lubricated regime EHD. The three

regimes can be distinguished using the non-dimensional Sommerfeld number, defined as $S = \eta VL/P_{eff}H^2$ where η is the fluid viscosity at the mean estimated surface temperature at steady state, V is the slip rate, P_{eff} is the effective normal stress, L is the characteristic slip length and H is the average height of the initial asperities. When $S < 10^{-3}$, the normal stress is supported by solid–solid contacts and the dynamic friction coefficient is close to the static friction coefficient. In the fully lubricated regime (EHD), when $S > 1$, the normal stress is supported by an interstitial fluid; and in the mixed lubrication regime (ML) when $10^{-3} < S < 1$, the normal stress is supported both by the solid–solid contacts and the fluid with the dynamic friction coefficient strongly reduced compared to the static one.

4. Acoustic fluidization (Melosh, 1996): the acoustic waves reverberating inside the granular material in the fault could have a frequency such that they could energize small grains such that they become fluidized and reduce their resistance to shearing.

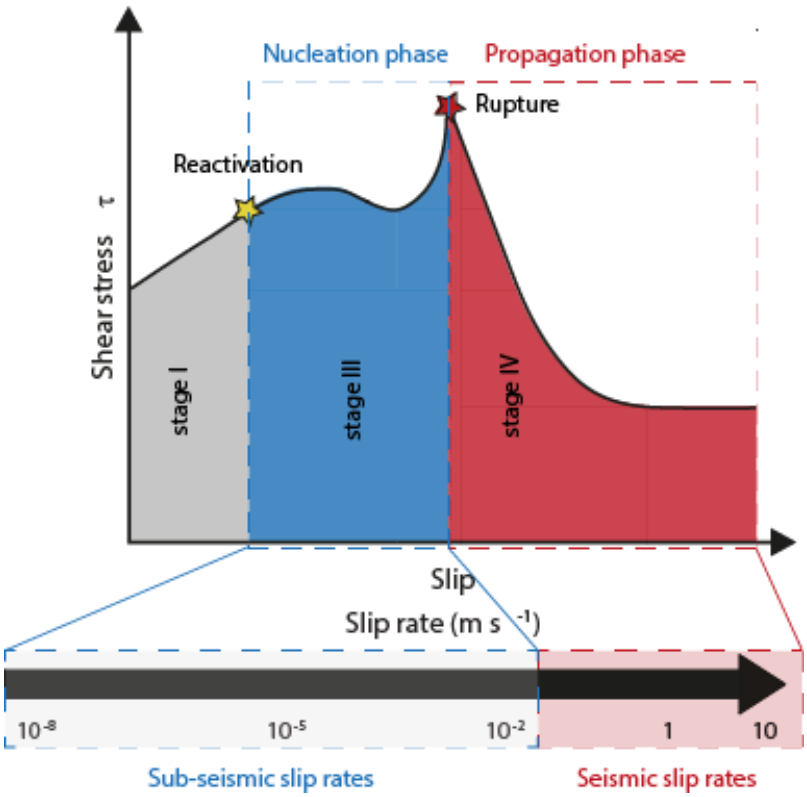

Figure 1: Schematic view of the stress change during the seismic cycle for both natural and induced earthquakes. Processes in the creation of an EGS reservoir are identical to those operative during a natural earthquake cycle. Faults respond to fluid-induced stress perturbations depending on their stability state by (stage I) remaining locked, by (stage II) undergoing slow and stable sliding (stage II is not presented in the figure because it represents an alternative scenario to stage III and IV and was not investigated in the EDGAR project), by (stage III) experiencing local on-fault short-lived unstable events (earthquake precursory sequence), or by (stage IV) accelerating towards catastrophic seismic slip (main event).

Within this project, via laboratory-based pilot studies, we investigated the entire seismic cycle at the laboratory scale. Especially, we installed and calibrated a new biaxial deformational apparatus and we performed various series of laboratory experiments to investigate the role of fluids in earthquakes reactivation, earthquakes nucleation and earthquakes propagation. We focused our attention in one of the five above mentioned key parameters which control the earthquake reactivation in geothermal reservoirs: fluid viscosity. We report final recommendation for next steps into research and into field stimulation to study the phenomena of fault reactivation and avoid fault rupture propagation with fluids more viscous than water. The complexity of the studied problem and the ambiguous behavior that the role of fluid viscosity showed at the laboratory scale did not allow us to express our results in a clear and unique formula for fluid reservoirs stimulation.

2 Work done and Results

2.1 Sample collection

We have used samples of Westerly Granite due to its well-studied nature, its fine grain size, its low porosity, and its low degree of alteration. In agreement with our industry partner, Geo-Energie Suisse SA, we have assumed that this granitic rock formation is an appropriate representative of an EGS reservoir host rock as expected in the Haute-Sorne location of the Canton of Jura. For details see Chapter 3 of *Mechanical behavior of lubricated faults during earthquake nucleation and propagation*, Cornelio, PhD-Thesis n. 7862 2020, EPFL.

2.2 Sample characterization

Mineralogical composition has been measured through X-ray diffraction analysis (Figure 2). Textural characterization has been checked by optical microscope. Porosity has been measured with a gas pycnometer, (porosity < 2%), and permeability at room pressure and temperature has been measured by both transient step method and oscillatory permeability methods.

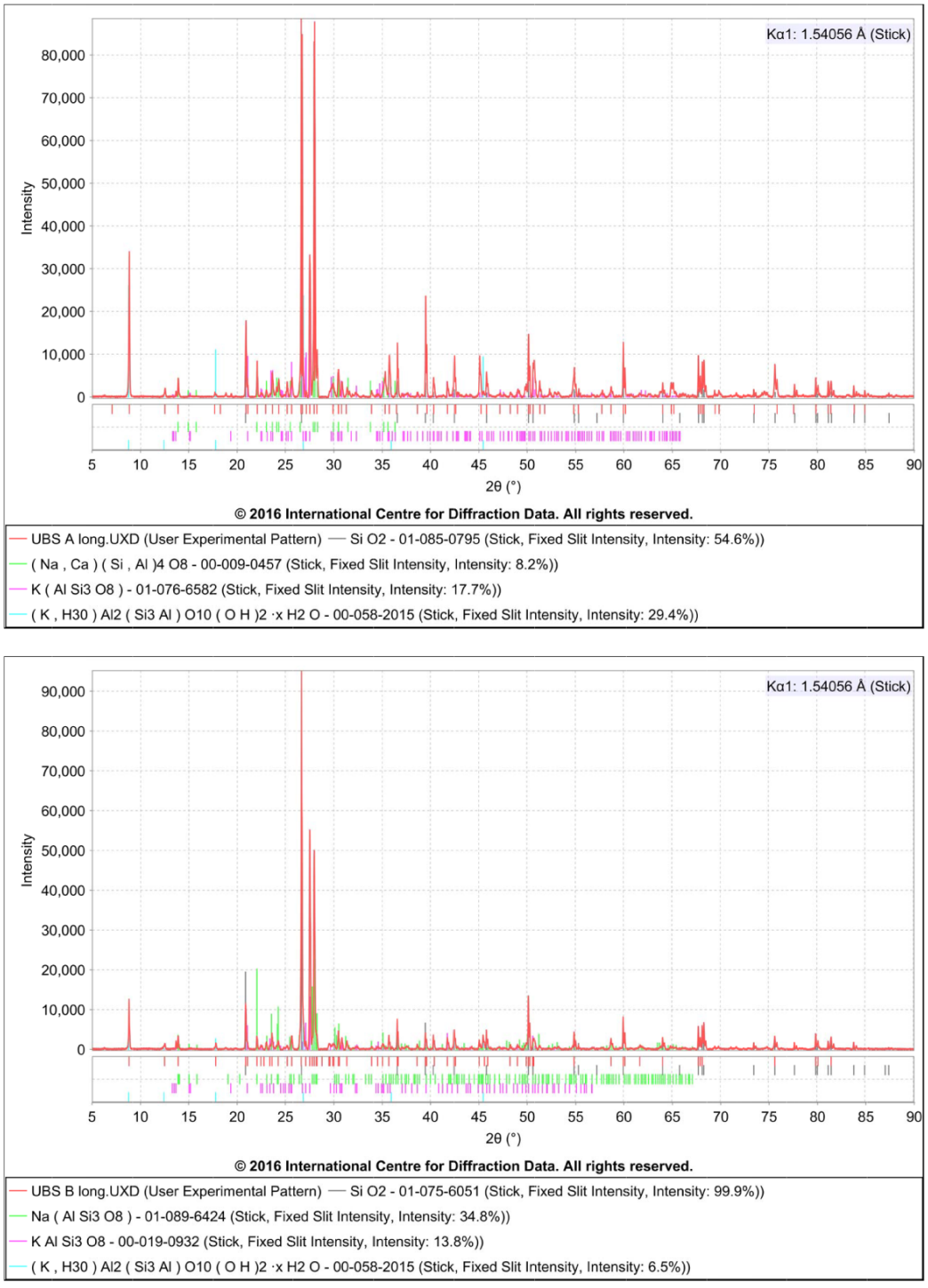

Figure 2: X-ray diffraction analysis of the used granite

2.3 HighSTEPS biaxial friction machine

The goal of the project *Fracture Design for Geothermal Reservoir* (EDGAR) is to investigate via laboratory based pilot studies the entire seismic cycle under conditions relevant to geothermal reservoir stimulation. To do so, we designed and built a state-of-the-art apparatus capable of applying unique

boundary conditions. Under these unique boundary conditions, we are able to reproduce the typical boundary conditions of geothermal reservoirs in terms of lithostatic pressure, pore fluid pressure, pore fluid physical and chemical properties, and temperature. Moreover, the high accuracy of the sensors and the high precision of the control allow us to investigate in unprecedented way the physical parameters controlling fracture reactivation in geothermal reservoirs (see paragraph 1). This laboratory studies will lay the foundation for the development of adequate procedures for reservoir engineering. In the following, we provide a detailed description of the novel apparatus developed in the context of this project.

2.3.1 Design of the apparatus

The rig is 1.90 m long, 0.7 m wide and 2.5 m high with a weight of around 3000 kg. The apparatus consists of a hydraulic system integrated with four linear motors (Figure 3). The normal stress is applied by a horizontal piston. The confining pressure is applied through an oil-confining medium by an intensifier connected to a vessel implemented within the biaxial frame. The pore fluid pressure is applied by two pore fluid intensifiers connected to the sample, which also allow for permeability measurements. In addition, the vessel is equipped with two heating plates and feedthroughs for acoustic sensors and strain gauges. The main uniqueness of this apparatus is the system of four linear motors mounted in parallel in order to subject samples to shearing velocities of up to 0.25 m/s, accelerations up to 10 m/s^2 and shear stresses up to 100 MPa, representative of conditions during seismic slip (Figure 1).

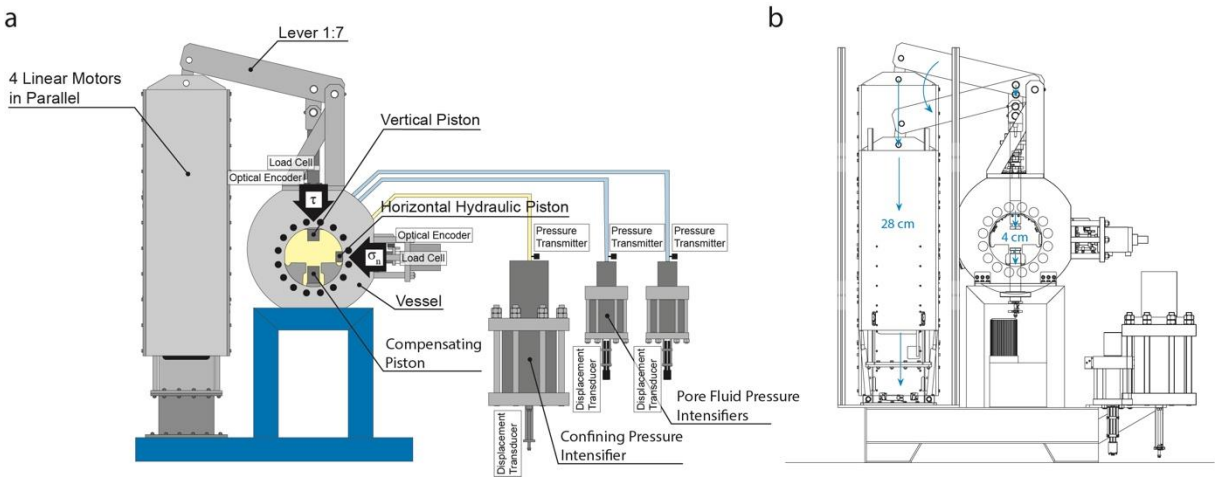

Figure 3 a) Schematics of the HighSTEPS apparatus. 4 linear motors are mounted in parallel to apply vertical force through a 1:7 lever. The vertical piston is equipped with an optical encoder and a load cell. The horizontal hydraulic piston applies a horizontal force and it is equipped with an optical encoder and a load cell. Two pore pressure intensifiers apply pore fluid pressure and they are equipped with displacement transducers and pressure transmitters. The confining pressure intensifier applies confining isotropic pressure and it is equipped with a displacement transducer and two pore pressure transmitters. The intensifiers are connected to the pressure vessel. b) Sketch of the working principle of the lever 1:7 that imposes the shear displacement and shear stress to the experimental fault.

2.3.2 The hydraulic power supply and oil circuit

The hydraulic power supply with a weight of 300 kg, has dimensions of 1400 x 850 x 900 mm^3 and is built by Polytec SAS located in Padua, Italy. The power supply is located in a room next to the laboratory, about 5 m away from the machine. It supplies oil pressure to the hydraulic intensifiers and piston of the machine and includes two oil pumps driven by a 7.5 W electrical motor, an oil tank, oil and air filters, a pressure accumulator to stabilize the pressure, pressure and level sensors, and finally an electro-valve allowing pressure regulation. The principal pump is characterized by a maximum pressure of 160 bars and a maximum flow rate of 23 l/min. The recycling oil pump is characterized by a maximum pressure of 8 bars and a maximum flow rate of 24.5 l/min respectively. The oil tank of a capacity of 75 l contains mineral oil and is connected to a cooling system composed of a chiller and a heat exchanger.

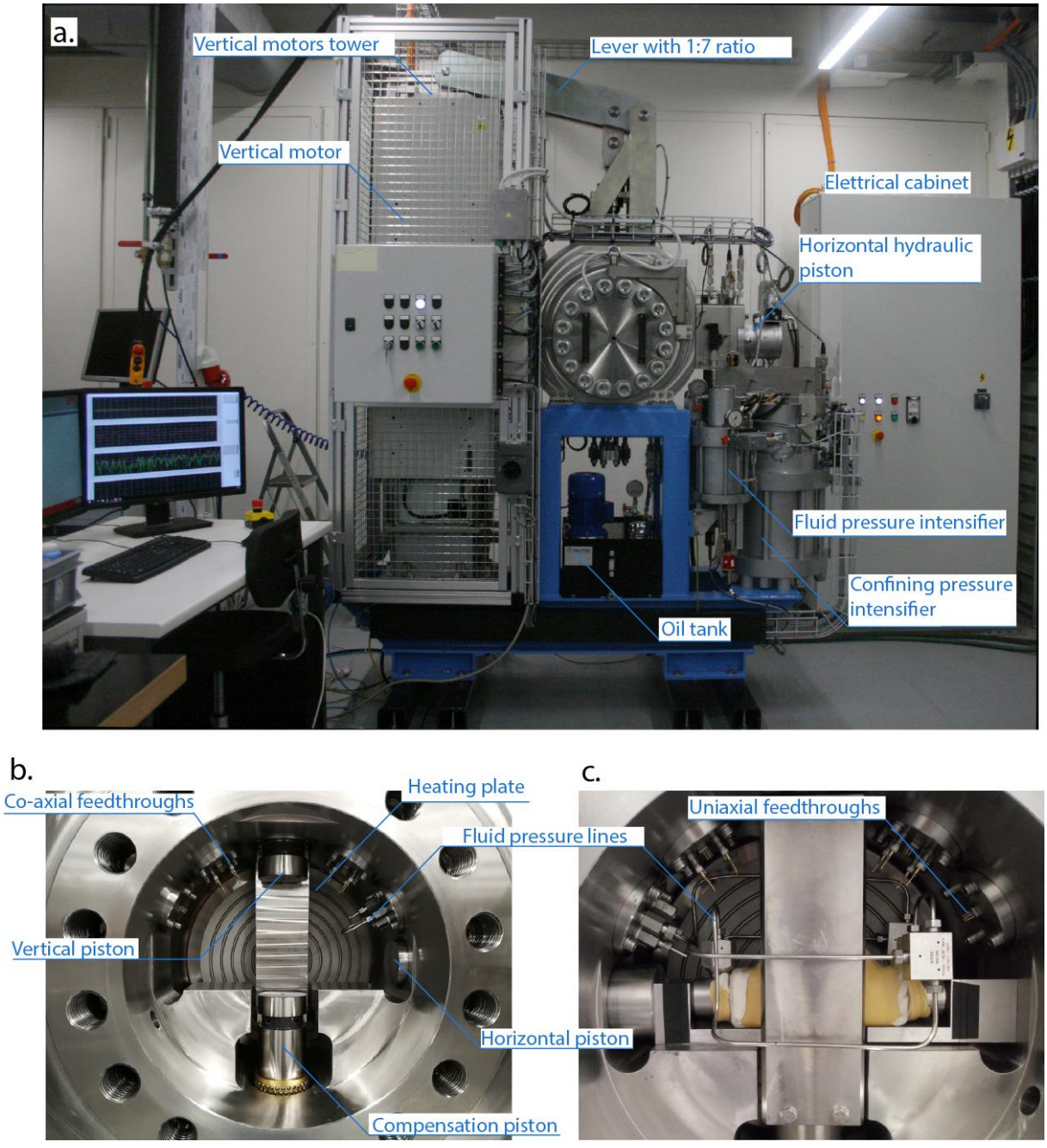

Figure 4. a) Picture of the highSTEPS machine, b) pressure vessel with high pressure ports for pore fluid and confining oil, and uniaxial and coaxial feedthroughs for electronics.

2.3.3 The three intensifiers and the hydraulic piston

The three pressure intensifiers and the hydraulic piston were also designed and built by Polytec, SAS (Figure 3a and 5a). They work with an entry pressure of 70-160 bar generated by the hydraulic power supply.

The horizontal hydraulic piston, with a stroke of 30 mm, is mounted on the pressure vessel and can exert a force up to 160 kN (Kilonewton). Horizontal force is controlled by a servovalve (MOOG D638-390-

0001 Type R02TO1M0HEE2MAOK1B1) mounted on the piston (Figure 5a). The piston is equipped with an optical encoder Renishaw (RL 26BSS005C30 A) mounted on a single-track scale (RSLA ABS) which allows displacement measurements with a resolution of 5 nm. The horizontal force is measured by a load cell (FUTEK LCM 550) located in the middle of the piston with a resolution ±0.03 kN over the range 0-220 kN.

Two intensifiers are used for fluid pressure generation up to 100 MPa, fluid flow up to 60 cm^3/min through the sample, and dilatancy and permeability measurements. Permeability can be measured by steady state, transient and harmonic flows methods. Fluid pressure is controlled by servo-valves (MOOG D633-592B Type R01KO1D0NSS2) mounted on the top of the intensifiers, and measured by a pressure transmitter (Gefran TSPA series) with a resolution of 100 kPa. The intensifier displacement is measured by two linear position sensors (TEMPOSONIC RP-V-0100M-D70-1-S1B1100) with a resolution of 0.5 µm. The intensifiers' volumes are 130 mm^3 each.

The third intensifier is used to apply oil confining pressure and has a larger volume than the pore fluid intensifiers, i.e., 1425.5 cm^3. Confining pressure is controlled by a directional valve (D DS3-S3/11N-D24K1) and a proportional valve (MZE4/58-24, MVPP-D/50, MERS-GD/50) fixed on the intensifier, to allow pressure generation up to 100 MPa. Confining pressure is measured by two pressure transmitters (Gefran TSPA series) with a resolution of 100 kPa, one located close to the intensifier, and the other one located close to the pressure vessel (Figure 5). Intensifier displacement is measured by a Gefran ICC150EM rectilinear displacement transducer with a stroke of 150 mm.

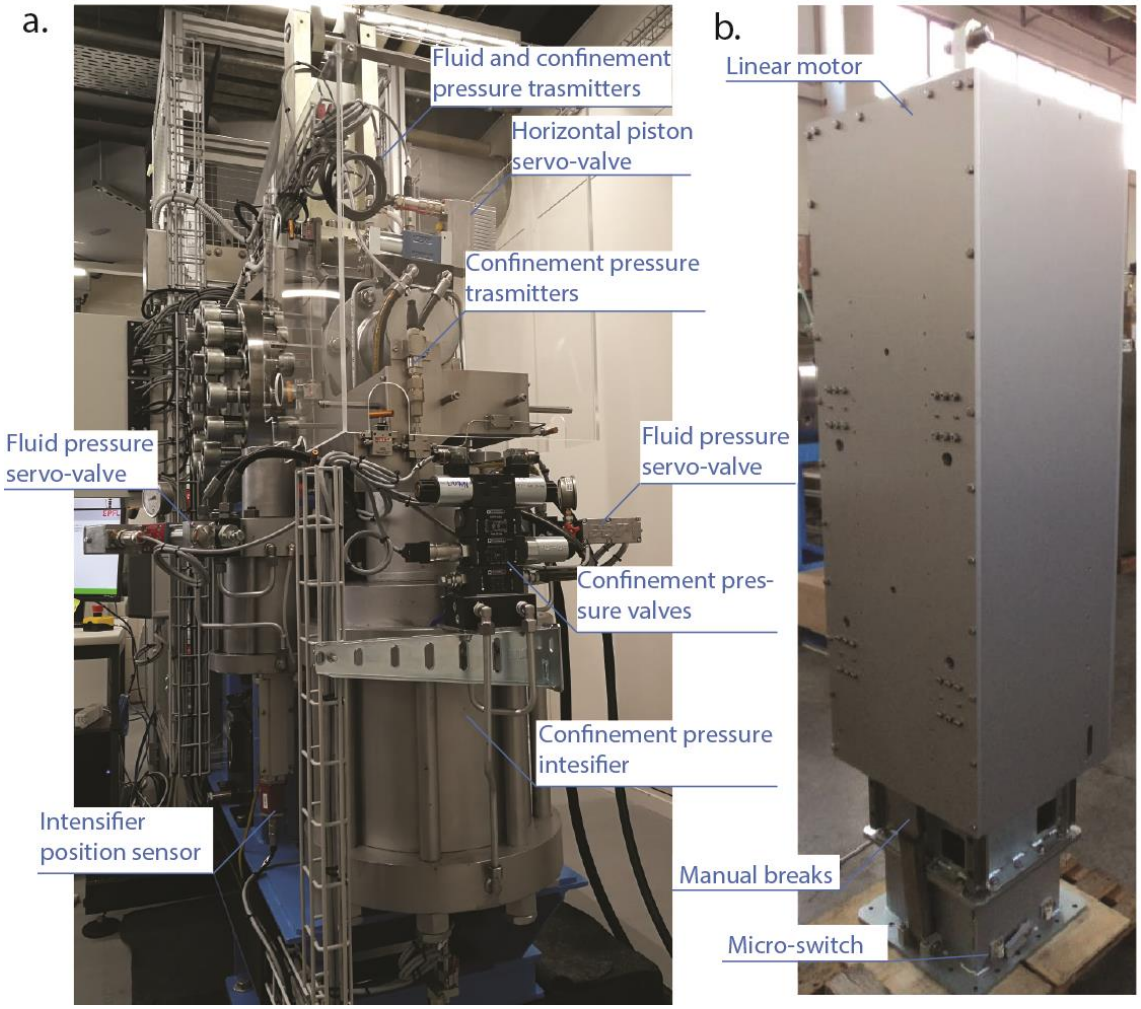

Figure 5: a) detailed of the intensifiers, b) details of the motors.

2.3.4 Pressure vessel

The pressure vessel was built by RMP S.r.l., located in Rome, Italy. It is made of stainless steel, weighs about 500 kg, and has an external diameter of 700 mm and an internal diameter of 300 mm (Figure 4b). It is designed to support 100 MPa confining pressure. The vessel supports the vertical and horizontal pistons. To close the vessel, two doors of 130 kg each, are equipped with 20 M36-size bolts. To ensure perfect sealing of the chamber, high-pressure and temperature dynamic seals are mounted on each door and on the pistons. To ensure easy opening and closing, doors are suspended on swing arms. Three pore pressure lines (two connected to one pore pressure intensifier and one connected to the other pore pressure intensifier) and one oil confining pressure line are connected to the pressure vessel. The pressure vessel is equipped with eight high pressure co-axial feedthroughs from Kemlon for acoustic sensors connection and 24 uniaxial feedthroughs for strain gauge connection, and 3 type K thermocouple feedthroughs (Figure 4b and c). Another access port located at the bottom of the vessel is used to fill and empty the vessel with the confining oil. The oil for confinement is a silicon oil supplied by Green Star High Tech Lubricants and Additives, stable to temperature up to 240 °C. The oil is contained within a tank equipped with a pump which is used to fill the pressure vessel above.

2.3.5 Heating system

The heating system, composed of two heating plates of 26 mm diameters with a high resistance, is fixed to the inner part of the vessel doors (Figure 4b and c). The maximum temperature of 120 °C is limited by the flash point of the confining oil and the temperature stability of the dynamic seals located on the vessel doors. Temperature is measured within the 2 heating plates and in the oil confining medium by 3 K-type thermocouples. Temperature is controlled with a potentiometer.

2.3.6 The four linear motors and vertical pistons

The motion of the vertical piston of the machine (applying the shearing velocity and shear force to the experimental fault) represents the most innovative aspect of the apparatus. It consists in four linear motors built by Kollmorgen, Type IC44-200 A3 AC TS C1, which are mechanically mounted and electrically connected in parallel (Figure 5b). These motors are controlled by four controllers (one master and 3 slaves; brushless drive KOLLMORGEN type AKD 48A-AKD-10038). Each motor is equipped with 1 optical encoder (Renishaw RL 26BAT050B30A) with a resolution of 50 nm mounted on a single track-scale RSLA ABS, for a total of 4 encoders (1 master and 3 slaves) used to control the displacement, velocity and acceleration of the vertical piston.

The Kollmorgen motors are frameless, permanent magnet, three phase, brushless servo motors composed of a coil assembly (also called the slider) and a magnet track (also called the magnet way). The mechanical support for the four motors is composed of a fixed frame where the coil assembly is screwed resulting in a total weight of 185 kg, and a moving part where 4 aluminum plates of 35 kg each are equipped with the permanent magnet tracks. A safety block composed of two manual breaks and micro-switches is fixed at the bottom of the frame and allows motor parking between the experiments. A second safety block, composed of two rigid springs, is fixed at the top of the frame and allows safe deceleration of the motors. The motors are water cooled during long-term experiments to avoid overheating of the magnetic coils. To turn on the motors, the machine is equipped with its own 125 A power panel. The connection between the motors and this panel is made by 4 electrical power cables and Ethernet cables for the four optical encoders (one for each motor). The four motors allow a nominal force up to 28 kN (6.9 kN each motor) and a peak force up to 37 kN (8.4 kN each motor), velocities from ~7 µm/s to 2.9 m/s and acceleration up to 70 m/s^2. The motors' control system is capable to impose complex displacement paths and time derivatives that result in velocity functions with a given acceleration, deceleration and target velocity.

The vertical piston driven by the linear motors is fixed on the pressure vessel and connected to the motors frame with a lever of a 1:7 ratio, allowing a maximum force applied on the sample of 193 kN with a maximum stroke of 5 cm. However, due to the lever, velocity and acceleration on the sample side are reduced to maximum 0.25 m/s and 10 m/s^2 respectively. The vertical piston is equipped with an optical encoder Renishaw (RL 26BSS005C30 A) mounted on a single track-scale RSLA ABS which allows displacement measurement with a resolution of 5 nm. The vertical force is measured and controlled thanks to a load cell (FUTEK LCM 550) located in the middle of the piston with a resolution ± 0.03 kN over the range 0-220 KN. The vertical piston located in the upper part of the vessel is equipped with a compensation piston in the lower part of the vessel, to avoid confining oil overpressure during fast movements. The compensating piston is mechanically connected to the vertical piston thanks to 2 metallic clamps inside the pressure vessel. During shearing experiments, the vertical piston moves

downward entering in the vessel and concurrently the compensation piston moves downward exiting the vessel, resulting in oil volume and oil pressure being kept constant inside the vessel during the entire experiment. Thanks to the compensation piston, which is connected to the vertical piston during the experiments, the confining pressure does not contribute in the vertical load measured by the load cell. The sample assembly is located in between the vertical and the compensation pistons.

2.3.7 Sample holders

Experiments can be carried out on both bare surface's samples and powdered samples, for which two different sample holders are used. The sample holders are designed for double-direct shear configuration and are composed of three forcing blocks of stainless steel: a central block of dimension 110 x 50 x 34 mm^3 and 2 side blocks of dimension 69 x 34 x34 mm^3 (Figure 6). A constant contact area of 34 x 20 mm^2 for bare surfaces and 34 x 34 mm^2 for rock powder is maintained constant during experiments. For experiments with powdered samples the forcing blocks are grooved allowing shearing within the sample and not at the boundary between the sample and the forcing blocks. For bare surfaces, the forcing blocks present housing of the exact size of the samples to keep well-aligned during shearing. The forcing blocks are equipped with high pressure fluid ports and channels allowing high pore fluid pressure experiment (Figure 6a), and permeability and dilatancy measurement during shearing. The two side blocks are also equipped with holes for piezoelectrical transducers, 9 mm in diameter. For experiments performed with confining pressure, the samples are isolated from the confining medium by using a double layer of latex jackets. This jacketing ensures limited biasing in terms of friction and can handle a large amount of deformation (maximum of 3 cm slip) before the jacket failure.

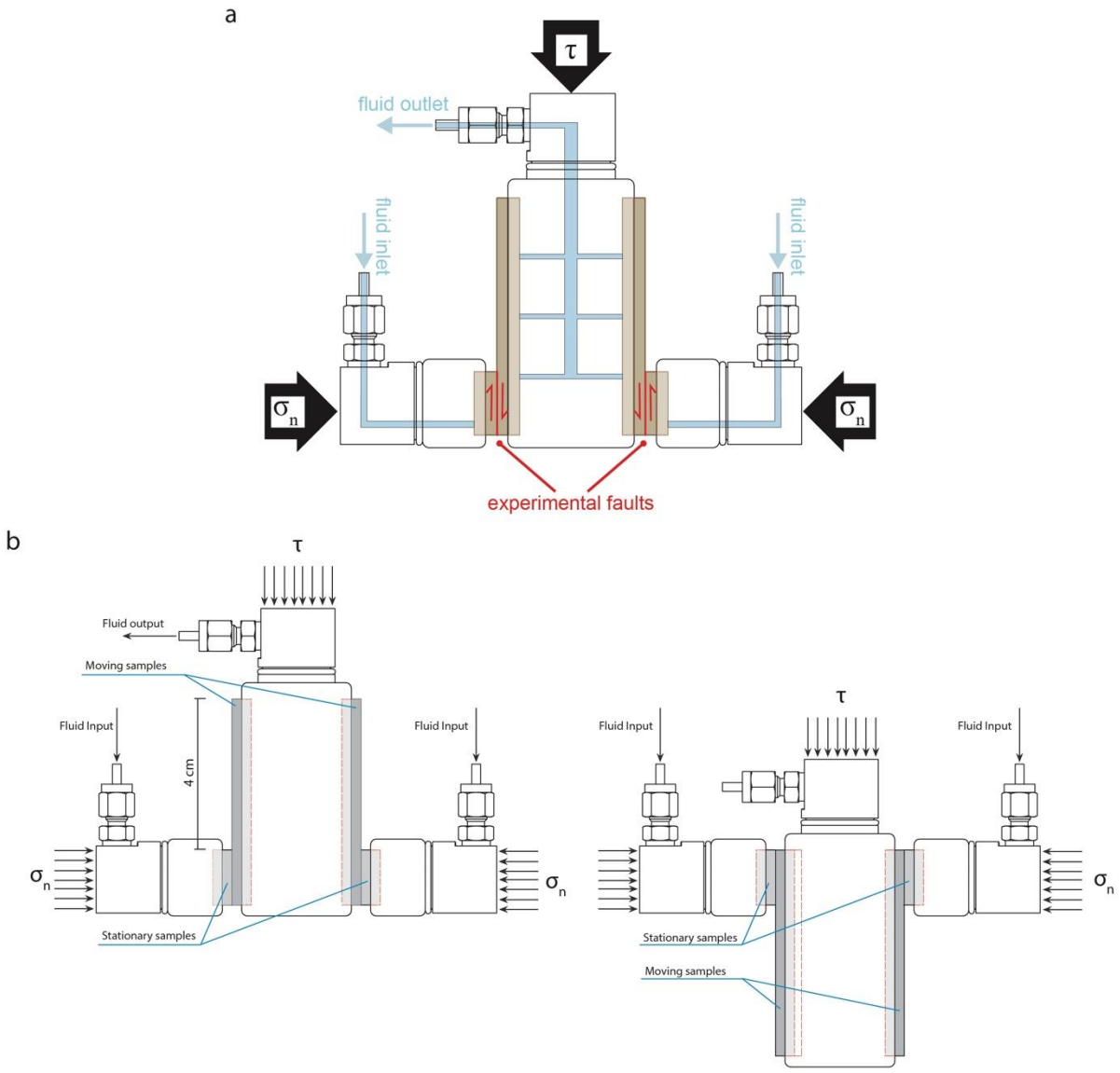

Figure 6. a) Schematics of the experimental double-direct-shear configuration. The sample holders are equipped with internal pore fluid channels for application of pore fluid pressure, injection of fluids and measurement of permeability/dilatancy of the fault rocks. b) Picture of the sample holder. c) Sketch of the working principle of the double-direct shear configuration.

2.3.8 Control and acquisition systems

The control and acquisition system was built by MEquadrat, based in Luzerne, Switzerland. It consists of a programmable automation controller, CompactRIO (National Instruments), which allows data acquisition at rates up to 50 kHz and real-time control of the normal stress, confining pressure, pore fluid pressure, temperature and slip velocity or shear stress, and 4 half-bridge strain gauges.
The vertical piston can be controlled in position (i.e., displacement of the experimental fault), velocity and force mode thanks to a closed loop servo control. The horizontal piston can be controlled both in position mode and in force mode thanks to closed loop servo control. The two pore fluid pressure

intensifiers can be controlled in position, flow, pressure mode. Thanks to the closed loop servo control, it is possible to impose sinusoidal oscillation of pore pressure. The confining oil pressure intensifier can only be controlled in pressure feedback servo control mode.

2.3.9 First test of the machine

1. Machine stiffness

To determine the apparatus distortion during deformation of samples, we deformed steel blocks of known stiffness (Young modulus E = 210 GPa) with both the vertical and horizontal pistons. We measured the resulting displacement of the apparatus by removing the contribution of the elastic deformation of the steel blocks (Figure 7). We performed the tests under room pressure and temperature conditions, imposing force steps of 1 kN at forces below 5 kN, steps of 5 kN at forces below 80 and 100 kN, for the horizontal and vertical piston respectively, and steps of 10 kN at higher forces. After reaching 160 kN, we performed steps down in force on the horizontal axis. Figure 7 shows the displacement versus load for both step-up and step-down measurements. Machine stiffness is defined as the slope of the linear regression between the points. Horizontal machine stiffness is 1786 kN/mm at load > 60 kN, vertical machine stiffness is 1379 kN/mm at load > 15 kN. Low stiffness at low normal stresses could be due to progressive closure of the interfaces between the steel block and the piston/vessel.

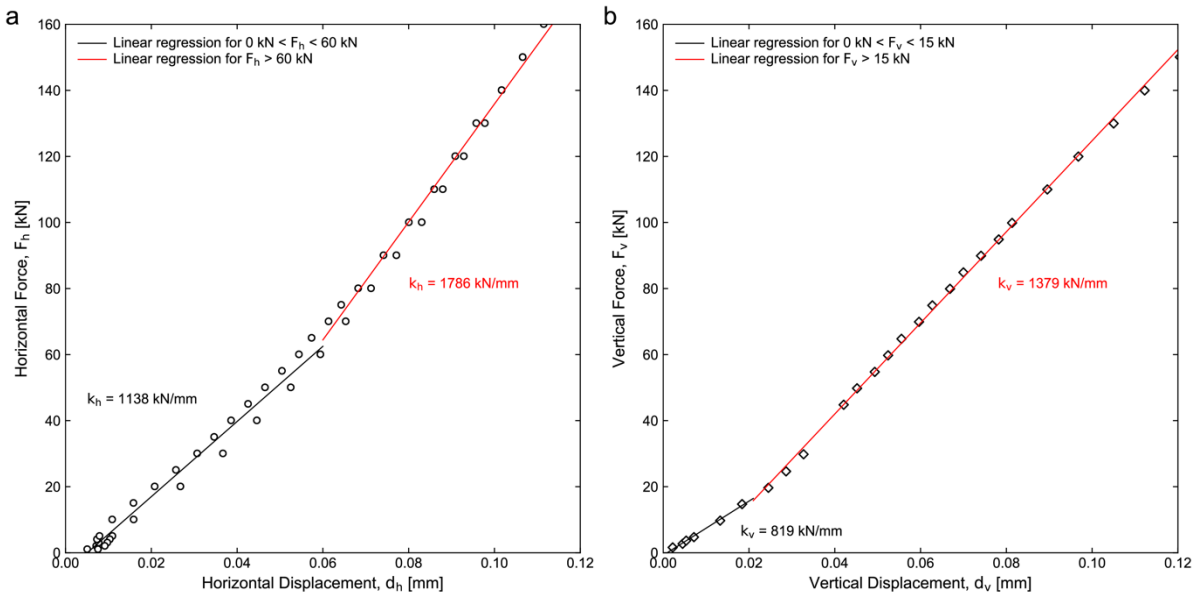

Figure 7: a) Horizontal and b) vertical machine stiffness measure with steel blocks. The horizontal stiffness is 1786 kN/mm for vertical force (F_h) higher than 60 kN. The vertical stiffness is 1379 kN/mm for horizontal force (F_v) higher than 15 kN.

2. Preliminary results on calcite and quartz

    a. Effect of normal stress

We used both gouge and bare surfaces of calcite (Carrara marble) to test the normal stress dependence of the frictional strength and compare the measurements performed with the new machine with previous experiments. Experiments were run under double-direct shear configuration for gouge and single direct shear for bare surfaces.

To produce calcite gouge, Carrara marble was crushed and sieved to < 200 μm in grain size. Gouge layers of 5 mm thickness were sandwiched between the grooved steel blocks (see paragraph 2.3.7). To produce calcite bare surfaces samples, Carrara marble slabs of 12 mm thickness were cut into pieces with dimension of 20 x 34 x 12 mm^3 and 70 x 34 x 12 mm^3, to ensure a 34 x 20 mm^2 constant contact area during shearing. The two surfaces in contact during the experiment were polished with a P60 grit SiC abrasive paper. Experiments were performed without confining pressure, under room temperature and nominally dry conditions.

The steady state friction coefficient was determined at a slip velocity from 33 μm/s to 33 mm/s and at normal stresses from 5 MPa to 50 MPa, for gouge, and at a slip velocity of 10 μm/s and normal stresses from 5 MPa to 12.5 MPa for bare surfaces.

The shear stress versus displacement curves for gouge sample at slip velocity of 6.6 mm/s are shown in Figure 8a. In all experiments, the shear stress first increased linearly with the displacement (i.e., elastic phase). Following elastic deformation, the shear stress showed a nonlinear decrease as a function of displacement (i.e., slip hardening phase) prior to peak stress. Then, following the attainment of peak stress, the sample sheared at a constant shear stress (i.e., steady state phase), except for the sample deformed at 50 MPa, that showed a slip softening phase after 5 mm displacement. Figure 8b shows the linear pressure dependence of calcite frictional strength (e.g., Byerlee, 1978). The steady state friction coefficient is obtained from the linear regression of the steady state shear stress versus applied normal stress and is 0.53 for bare surfaces and 0.50 for gouge. The intercept of the linear regression shows the negligible cohesion of the bare surfaces (0.44 MPa) and the gouge (0.88 MPa). The steady state apparent friction during experiments at low velocity (3.3 and 33 μm/s) and 10 MPa normal stress is $\mu \approx 0.6$ in agreement with previous studies (Verberne et al., 2014; Carpenter et al., 2015, 2016). Increasing the velocity to 6.6 cm/s, the apparent friction of calcite slightly decreases to values $\mu \approx 0.50$-0.55, as expected based on the rate-and-state friction law for velocity weakening rocks (Marone, 1998; Marone and Saffer, 2015; Moore and Lockner, 2011) and on previous observations (Violay et al., 2014; Pozzi et al., 2019).

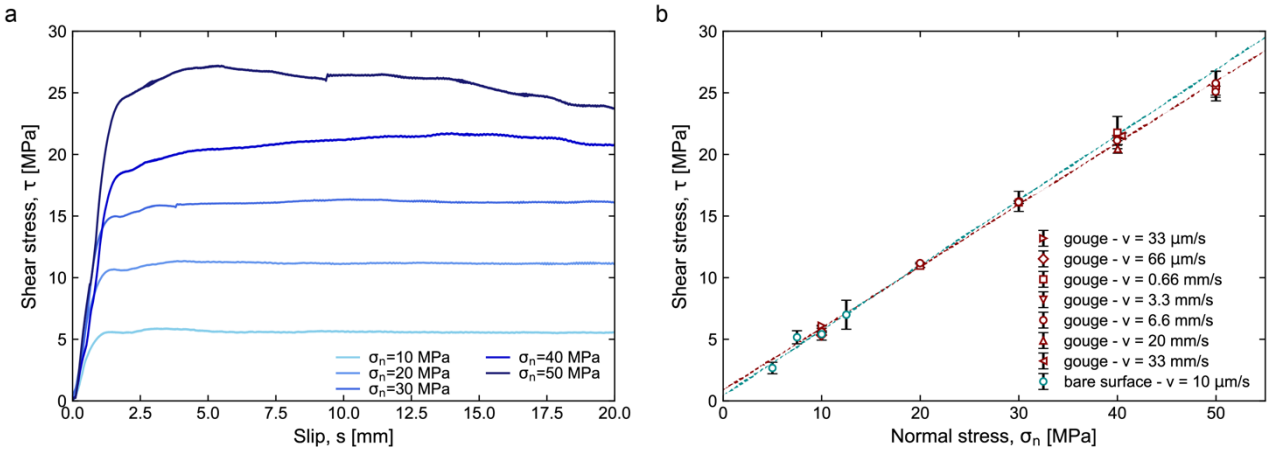

Figure 8: Calcite (Carrara marble) gouge and bare surfaces frictional experiments: a) shear stress versus slip during frictional sliding at v = 6.6 cm/s and normal stresses from 10 MPa to 50 MPa. Experiments were performed under double-direct shear configuration on gouge material. d) Steady state shear strength versus normal stress for both gouge material and bare surfaces. Data plot along a single line with a slope of ~0.5, in agreement with Byerlee's rule (Byerlee, 1978).

b. Effect of velocity

Faults respond to velocity perturbations depending on their stability state. Faults may remain locked (stage 1), undergo slow and stable sliding (stage 2), experience local on-fault, short-lived unstable events (earthquake precursory sequence) (stage 3), or accelerate toward catastrophic seismic slip (main event) (Kaneko et al., 2010) (stage 4). The transition from stage 1 to 2, 3 or 4 controls the slip behavior during fault reactivation, i.e., the earthquake potential of a fault.

Rate-and-state friction (RSF) laws provide a comprehensive framework to interpret a fault's slip behavior. In this framework, the frictional response of a fault varies with the previous loading history and depends on both, the imposed loading (instantaneous slip velocity, normal stress) and a state variable that describes the progressive evolution of the sliding interfaces (Dieterich, 1972; Ruina, 1983; Dieterich and Linker, 1992):

Depending on the frictional evolution in response to an instantaneous change in slip velocity or normal stress, the rate-and-state law characterizes the capability of a fault to nucleate earthquakes or to creep aseismically. In the framework of rate-and-state friction, frictional resistance τ of the fault as a function of the slip rate v is given by

$$\mu = \mu_0 + a \ln\left(\frac{v}{v_0}\right) + b \ln\left(\frac{\theta v_0}{D_c}\right) \quad (1)$$

$$\frac{d\theta}{dt} = 1 - \frac{v\theta}{D_c} \quad (2)$$

where μ_0 is the steady-state friction at velocity v_0, a and b are empirical parameters, θ is a state variable which can be interpreted as the average age of the population of contacts between two surfaces, and Dc is the characteristic slip distance (i.e., the sliding distance required to renew the frictional contact population on the fault following a velocity step) (Dieterich, 1979; Ruina, 1983). To perform the stability analysis, these constitutive equations (i.e., Equations 1 and 2) are coupled with the

description of the elastic coupling between the fault and the elastic surrounding. When friction decreases following an instantaneous increase in slip velocity, (*a*-*b*) is negative and the behaviour is defined velocity-weakening. Contrarily, when friction increases following an increase in slip velocity, (*a*-*b*) is positive and the behaviour is defined velocity-strengthening. In this framework, a velocity-weakening fault is prone to nucleate instabilities, while a velocity-strengthening fault stably and slowly slips. The rate-and-state friction laws successfully reproduce fault behaviour during the entire seismic cycle, from precursory slip, earthquake slip, coseismic rupture and afterslip (e.g., Tse and Rice, 1986; Dieterich and Kilgore, 1996; Wennerberg and Sharp, 1997), and are used to model observed behaviour in natural faults (e.g., Veedu and Barbot, 2016).

Stage 4 controls earthquake propagation. During this stage, the slip velocity and power density (shear stress divided by velocity) increase drastically, inducing strong fault frictional weakening. Frictional weakening is controlled by a number of processes, such as flash heating and melting (Rice, 2006), decomposition reactions (Han et al., 2007), and superplastic flow and thermal pressurization (Violay et al., 2015). Many of these processes are actually thermally triggered (Di Toro et al., 2011 and references therein). (1) How the transition from slow slip velocity (slip velocity ~µm/s) to high velocity weakening behavior (slip velocity > cm/s) occurs, and (2) the conditions that drive faults through the aforementioned stages 1 to 4 are currently not clear.

The HighSTEPS apparatus covers slip velocities from µm/s to m/s (i.e., stages 1 to 4), enabling the measurement of the rate-and-state friction parameters and friction evolution during fault weakening and lubrication. Therefore, a complete collection of the mechanical data that are required to assess a constitutive equation for rock-friction will be possible. In Figure 9, examples of a single velocity step (Figure 9b), slide-hold-slide sequence (Figure 9a), high velocity friction experiment (Figure 9c) and shear stress control experiment (Figure 9d) are shown.

Slide-hold-slide sequences are performed to measure frictional healing after a period of hold and thus to simulate fault re-strengthening during the inter-seismic phase. During this sequence, calcite gouge layers were sheared at a constant velocity of 10 µm/s followed by a hold period (t_h) during which the vertical ram stopped and gouge layers were under quasi-stationary contact. The slide-hold-slide sequence was conducted under wet conditions ($CaCO_3$-equilibrated water). The hold periods showed in Figure 9a are 30, 100 and 300 s. After each hold period, the gouge was re-sheared at 10 µm/s, as is shown in Figure 9a. We observe an increase of friction upon re-shear, followed by a decay to the previous steady state value. This difference in friction between the peak and the steady state ($\Delta\mu$) is defined as the frictional healing and is typical of granular gouge material (e.g., Marone, 1998; Richardson and Marone, 1999). The frictional healing rate $\beta = \Delta\mu/\Delta\log_{10}(t_h)$ measured for calcite gouge under wet conditions is $\beta = 0.029$ and is in agreement with previous work (e.g., Giorgetti et al., 2015; Carpenter et al., 2016).

The velocity step was performed on quartz gouge with grain size < 125 µm/s (Fig. 6b) and showed an abrupt change in friction (the “direct” effect, “a” parameter in rate-and-state laws) and a pronounced evolution effect (the parameter “b” in rate-and-state law). The resulting negative a-b value is in

agreement with previous studies on quartz gouge (e.g., Marone, 1998; Marone and Saffer, 2015; Moore and Lockner, 2011).

High velocity friction experiments were performed on calcite bare surfaces at slip rate of 0.2 m/s, acceleration and deceleration of 5 m/s^2 and normal stress of 10 MPa. Once the velocity function was applied, the sample initially deformed elastically (i.e., the shear stress increased linearly with time), until the static friction was overcome and slip on the sample initiated. Consistent with previous experimental observations, the shear stress decayed towards a steady state friction value of 1 MPa corresponding to a steady state friction coefficient of 0.2 (e.g., Violay et al., 2014).
The vast majority of previously described experiments, either under slow or high slip velocity, has been conducted by imposing velocity functions. However, a more realistic boundary condition is to describe fault loading in terms of the forces and resulting stresses acting on a fault, whether virtually constant, slowly increasing due to tectonic loading, or increasing/decreasing in sudden steps (stress transfer) due to ruptures in the vicinity of the fault. Thus, in experimental practice, controlling the shear stress and allowing the slip velocity to adjust spontaneously, rather than the contrary, is closer to natural conditions where the "far field" stress, together with the frictional properties of the fault materials, controls the mechanical response of the fault zone. This type of loading also allows to track the evolution of normal stress during slip, and when coupled with volumetric strain measurements enables the evolution of porosity and permeability with slip – one of the key parameters that will govern how a fault stimulated by injecting stimulation fluids will respond, ideally in an aseismic or controlled seismic manner.

To this end, HighSTEPS is able to impose up and down shear stress steps. Figure 9d shows an experiment conducted in shear stress control mode. Initially, the calcite gouge sample was deformed under double-direct shear configuration at constant velocity of 10 µm/s and normal stress of 20 MPa, room pressure and temperature condition, until the steady state shear stress was achieved and the fault accumulated 10 mm of displacement. Then we switched the control mode to shear stress, and the shear stress was gradually increased by small (0.5 MPa) stepwise increments. The response to the loading is measured in terms of slip velocities. After each shear increment, we waited until either a quasi-static balance or a steady-state sliding was achieved before applying of the next stress increment. The process was repeated until the onset of the main instability, that is, the catastrophic acceleration of slip to 100 µm/s. We observe slip pulses which develop right after the instantaneous shear stress increase. During the last stress step, the fault gouge spontaneously evolved from primary, to secondary, and tertiary creep (Kassner and Pérez-Prado, 2004).

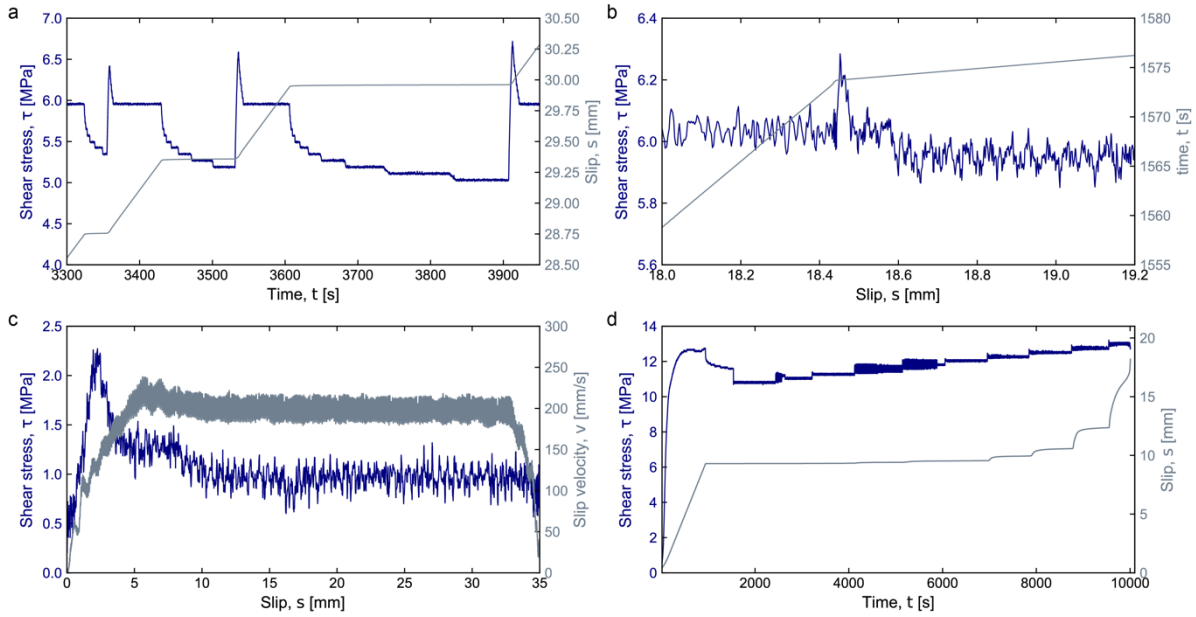

Figure 9: Example of velocity control and shear stress control experiments performed: a) slide-hold-slide test performed on calcite gouge at 10 MPa normal stress under room temperature and wet conditions; b) velocity step test on quartz gouge at 10 MPa normal stress under room temperature and room humidity conditions; c) high slip velocity friction test on calcite bare surface at 10 MPa normal stress under room temperature and room humidity conditions; d) shear stress control test on calcite gouge at 20 MPa normal stress under room temperature and room humidity conditions

c. Test with the pressure vessel, temperature and pore fluid pumps

First tests with the pressure vessel, temperature and pore fluid system have been performed without shearing motion. Figure 10 shows that the vessel and the pore fluid pumps can support pressure up to 80 MPa testifying the accurate control of these parameters including that of temperature.

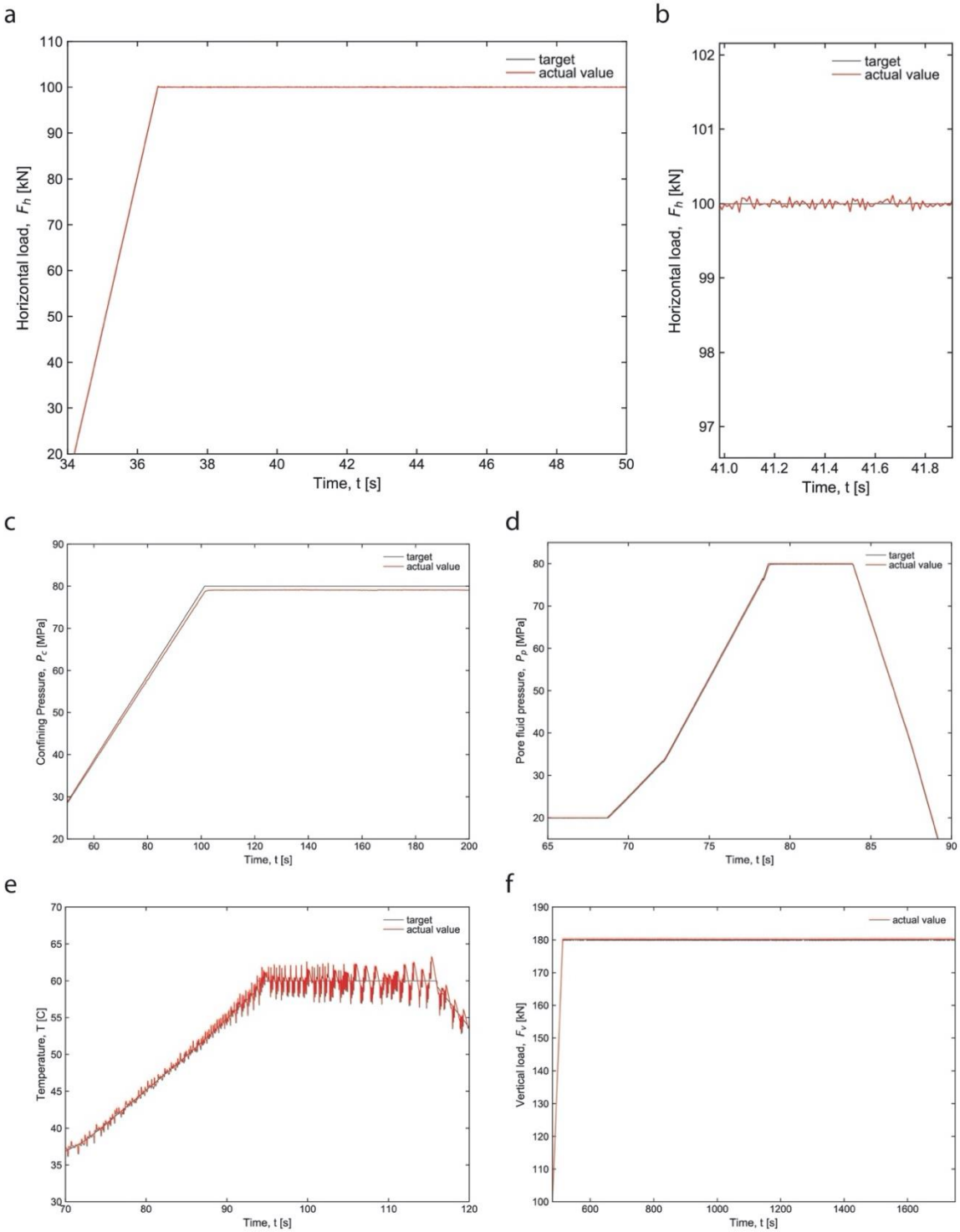

Figure 10: Tuning of the experimental parameters. a) Horizontal load versus time showing the control of the piston in force ramp (kN/s) and constant force (100 kN). b) Detail of a) showing the signal perfectly following the target. c) Confining pressure versus time showing the control in pressure up to 80 MPa. d) Pore fluid pressure versus time showing the control in pore fluid pressure. e) Temperature versus time showing the control in temperature up to 60 °C. f) Vertical force versus time showing the control in vertical force up to 180 kN.

2.3.10 Future machine development

We are currently finalizing the design of the jacketing system that will allow us to run experiments under both low and high slip velocities, high confining pressure, high pore pressure and high temperature. Using this jacketing system, we will be able to measure fault dilatancy and permeability. This new jacketing system will also allow to use up to 8 acoustic sensors glued directly on the rock samples and up to 4 quarter-bridge strain gages. With this new equipment, we aim at better understanding the evolution of frictional properties of fault rocks over the entire seismic cycle, going from long inter-seismic period, earthquake nucleation to propagation.

2.3.11 Summary

We have demonstrated that HighSTEPS is capable for experiments that shed light on the behavior of faults subject to hydraulic stimulation under a range of loading conditions.

2.4 Frictional tests

Various series of frictional experiments have been performed to understand the role of fluid viscosity on the mechanical behavior of faults. These experiments were run in order to simulate at the laboratory scale the injection of fluids into a geothermal reservoir crossed by fault a different state of stability. Experiments have been performed on granite sample because representative of swiss deep geothermal reservoirs.

2.4.1 STEP 1: Slip velocity tests - High speed friction tests with viscous fluids

Experimental procedure

Experiments have been performed in rotary shear configuration (Figure 11) at the Istituto Nazionale di Geofisica e Vulcanologia (INGV) Rome in close collaboration with Prof. Di Toro in anticipation of the arrival of the HighSTEPS friction machine. The experiments were performed exclusively at room temperature with the slip velocity as the control variable. We conducted high speed friction tests on saw-cut Westerly Granite samples under drained pore water pressures of 2 MPa. Experiments were performed on both dry and fluid-permeated rocks, at normal effective stresses up to 10 MPa, with a slip-rate ranging between 10 μm/s and 1 m/s. Four different fluid viscosities were tested: distilled water (η~1 mPa s) and three mixtures of water with glycerol concentrations of 60%wt., 15%wt. and 0.1%wt. (η=10.8, 109.2 and 1226.6 mPa s, respectively). Details of the performed experiments are reported in Supplementary Table 1 of Cornelio et al. (2019) (see reference in paragraph 6).

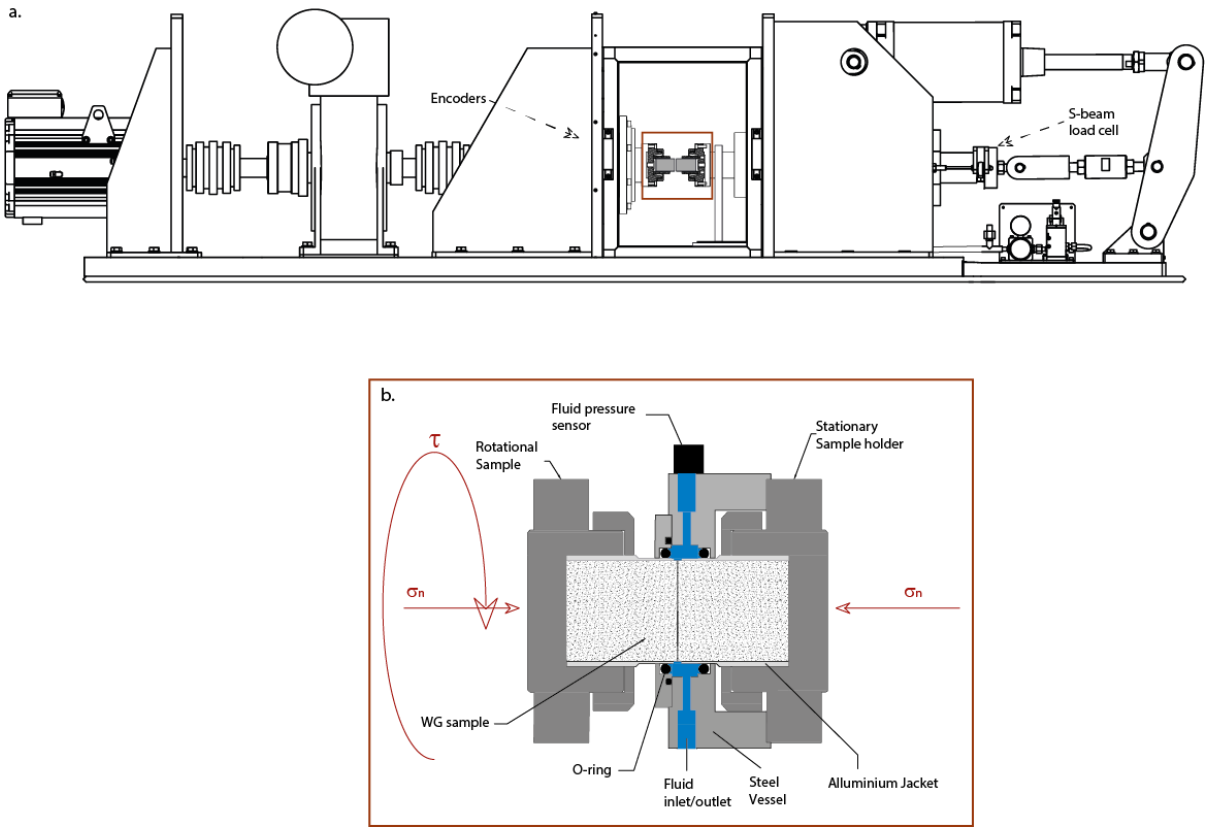

Figure 11: Experimental rotary apparatus SHIVA installed in INGV, Rome. Figure modified from Cornelio et al. (2020a) (see reference in paragraph 6).

Results

From the evolution of the ratio between the imposed normal stress on the fault and the measured shear stress on the slip plane, we can distinguish three frictional coefficients (Figure 12a). They are the static friction coefficient μ_{static} (i.e. the value of friction coefficient until slip initiates), the peak friction coefficient μ_{peak} (i.e. friction coefficient when the fault start to show a strengthening or weakening behavior), and, lastly, the dynamic or steady state friction coefficient μ_{dyn} (i.e. minimum and almost constant value of σ'_n over a slip distance D_c).

The results show that both static and dynamic friction coefficients decrease with viscosity (Figure 12b). Importantly, the dynamic friction depends on the dimensionless Sommerfeld number ($S=[6\eta VL]/[H_0^2 \sigma_{eff}]$, where η is the viscosity, V the slip velocity, and σ_{eff} the effective normal stress. We refer the reader to the sketch in Figure for the interpretation of the geometrical parameters L and H_0 as formulated in the elasto-hydrodynamic lubrication (EHD) theory. Details on the EHD theory can be found in Cornelio et al. (2019) (see reference in paragraph 6). The μ_{peak} was 0.651 ± 0.222 (highly scattered) over the entire range of S (Figure c).

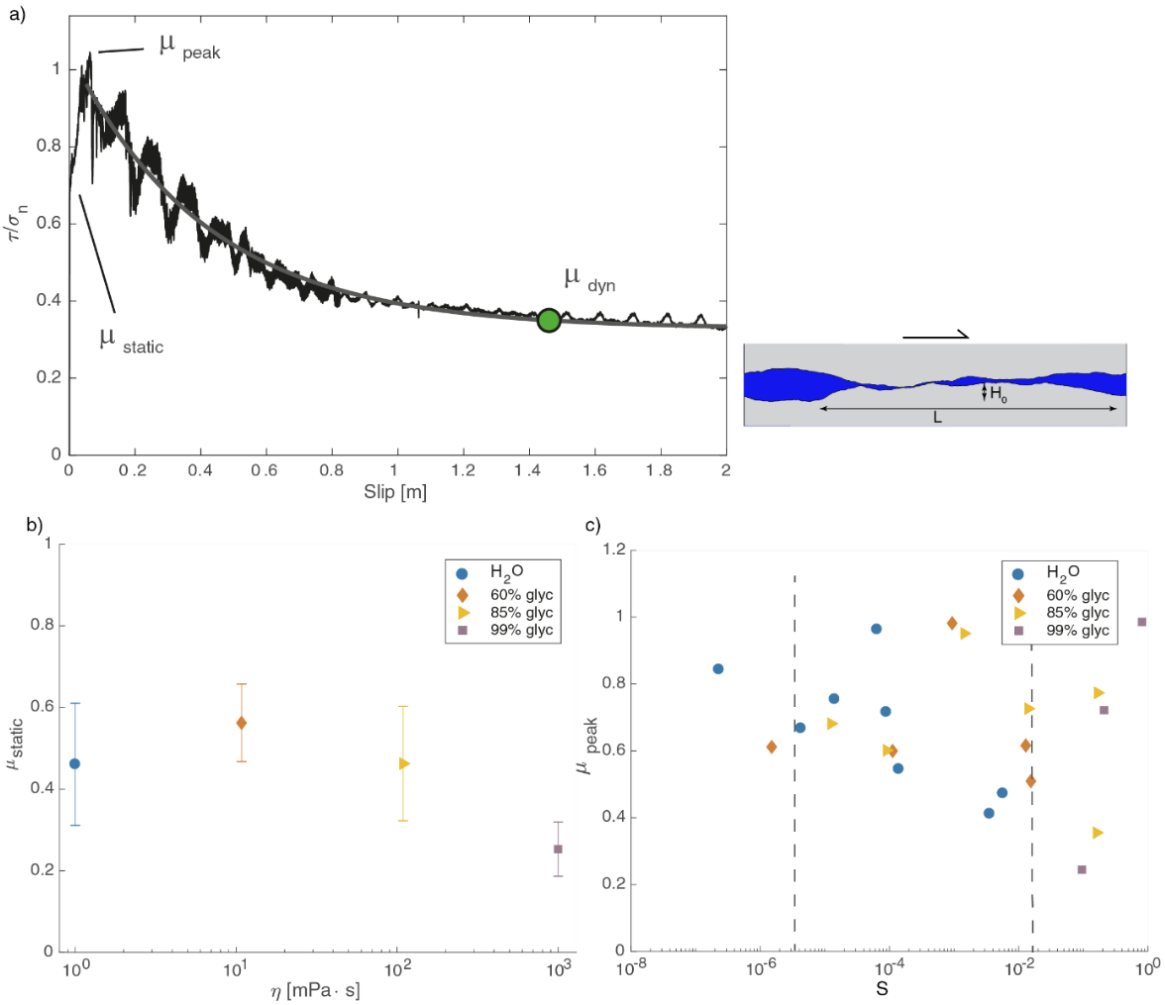

Figure 12: Apparent friction coefficients versus slip, friction coefficients versus viscosity η, and Sommerfeld number $S = 6 \cdot V \cdot \eta \cdot L/(P_{eff} \cdot H_0^2)$. Experiments were performed at an acceleration of $7.8\ m \cdot s^{-2}$ and effective normal stress σ_{eff} up to 20 MPa, under the following environmental and hydraulic conditions: 100% water (H_2O, blue dots), 60% glycerol/40% water (orange diamonds), 85% glycerol/15% water (yellow triangles) and pure glycerol (99% glycerol, purple squares). a) Apparent friction coefficient versus slip (S1315) experiment performed at $\sigma_{eff} = 10$ MPa in the presence of mixture 60% glycerol/40% water. μ_{static}, μ_{peak}, μ_{dyn} and Dc are represented. The apparent friction coefficient is fitted following the exponential decay function proposed by Mizoguchi et al. 2007[25]: $\mu = \mu_{dyn} + (\mu_{peak} - \mu_{dyn})e^{\ln(0.05)\, d/D_c}$ (grey line). b) Static friction coefficient versus viscosity η. In the semi-logarithmic scale, the static friction coefficient decreases linearly with increasing η. c) Peak friction coefficients versus Sommerfeld number. Figure modified from Cornelio et al. (2019) (see reference in paragraph 6).

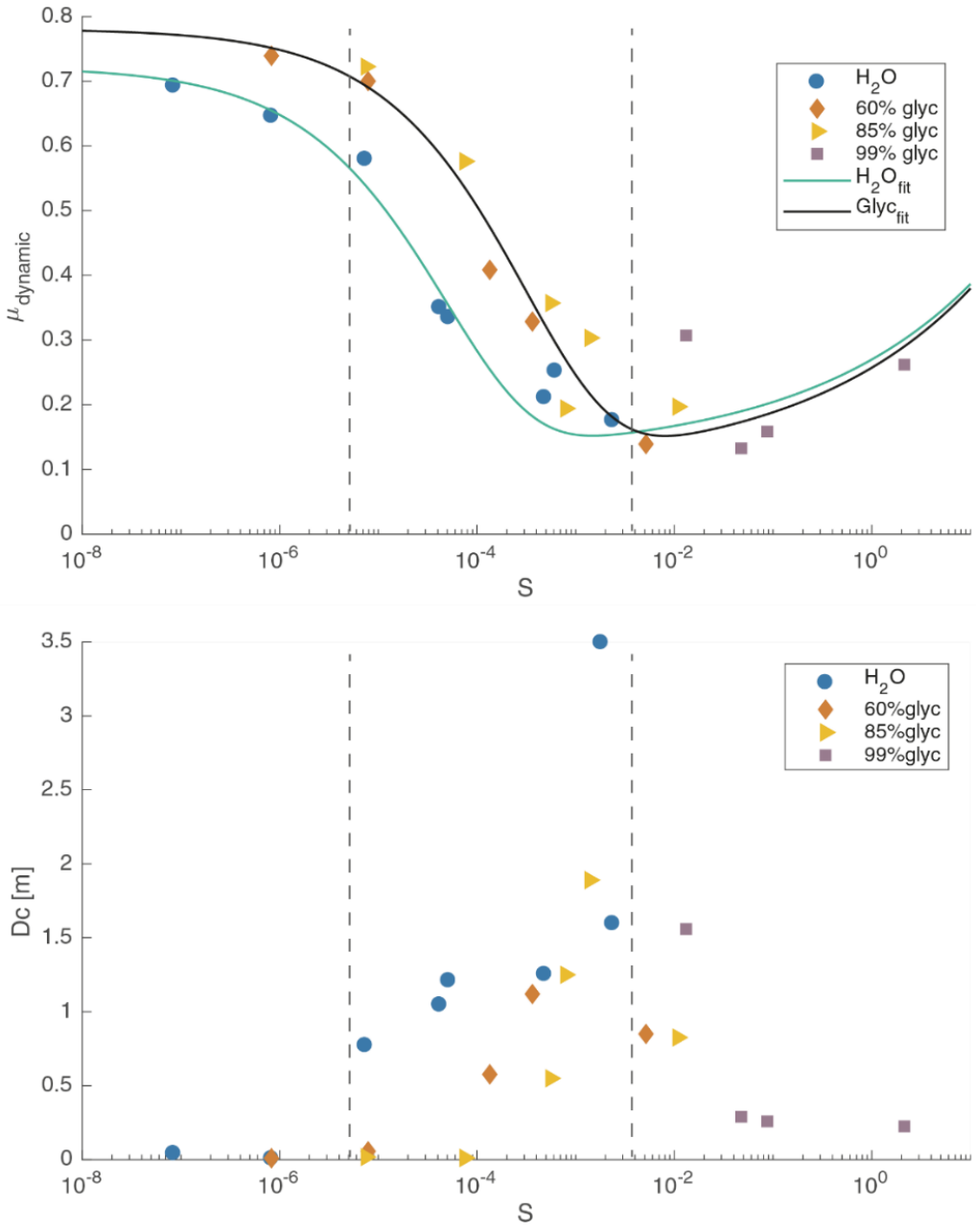

Figure 3: Dynamic friction coefficient and Dc versus Sommerfeld number S (same experiments and symbols as in Figure 12a). a) For $S< 10^{-5}$, the dynamic friction coefficient is independent of S. For $10^{-5} < S < 10^{-2}$, the dynamic friction coefficient shows a strong decrease with increasing S. For $S> 10^{-2}$, the dynamic friction increases with S. The fitted curves are obtained using Equation 1 in Cornelio et al. (2019) (see reference in paragraph 6) with coefficients of determination of R^2=0.95 and R^2=0.87 for the results obtained with the distilled water and glycerol mixtures, respectively. b) In the semi-logarithmic scale, the weakening distance D_c increased linearly in the logarithmic scale with S for the experiments performed in the presence of water and exponentially in the logarithmic scale with S in the presence of glycerol.

Interpretation

Extrapolation of our results to crustal conditions suggested that EHD is an effective weakening mechanism during earthquakes. It is likely that this mechanism will be also operative during large-scale hydraulic stimulation of the Earth's crust. However, at seismic slip-rates, the slip weakening distance (Dc, Figure 3) increases markedly for a range of fluid viscosities expected in the Earth, potentially favoring slow slip rather than seismic propagation for small to moderate seismic events. Slow slip is in principle beneficial during hydraulic stimulation because of the possibility to substantially lower the likelihood of large, sudden stress drops during seismic slip.

Modeling of the energy budget and computed energy radiated from our experimental results suggested that the excess of energy available for rupture propagation decreased linearly with increasing Sommerfeld number S in both the boundary and mixed lubricated regimes. Therefore, in the presence of high viscosity fluids, transition from slow nucleation to seismic propagation could not occur until rupture indicatively reaches kilometric lengths.

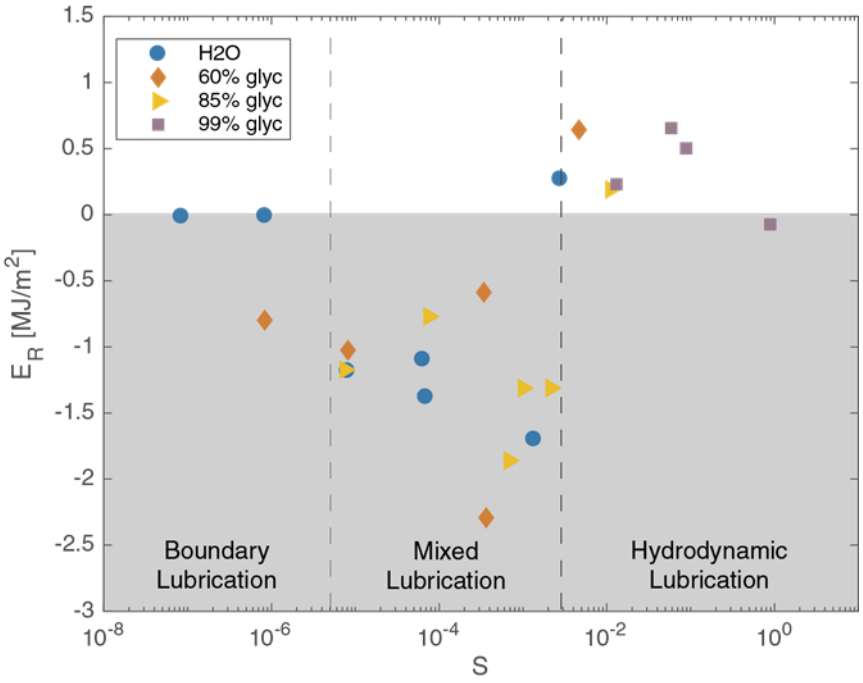

Figure 4: The excess energy available for propagation of the rupture and wave radiation E_R versus Sommerfeld number for the three lubrication regimes delimited by the black dashed straight lines (same experiments and symbols as in Figure 13). The excess of energy available for rupture propagation decreased linearly with increasing Sommerfeld number S in both the boundary and mixed lubricated regimes. For $E_R<0$ (grey area), there is no rupture propagation, for $E_R>0$ there is seismic rupture, and for $E_R\sim0$ there is quasi-static rupture.

The experimental procedure, results and discussion for the experiments presented in this section have been published in Nature Communication journal (Cornelio et al. 2019) (see reference in paragraph 6).

2.4.2 STEP 2: Velocity steps experiments with viscous fluids

Experimental Procedure

Velocity step experiments have been performed on granite saw-cut samples using a particular configuration suitable for a triaxial deformation apparatus (Figure 15). The change in friction as a direct response of the fault to velocity step perturbations has been studied on the framework of rate and state dependent friction. Experiments were performed under ambient humidity conditions as well as in the presence of fluids with various viscosities. Two effective normal stress (σ_N) acting on the faults were tested (30 MPa and 50 MPa), while the fluid pressure (P_f) was kept constant during the experiments. The ratio P_f/σ_n was kept constant and equal to the one used in the first series of experiments $P_f/\sigma_N=1/6$. The list of the experiments performed can be found in Cornelio and Violay (2020c) (see reference in paragraph 6).

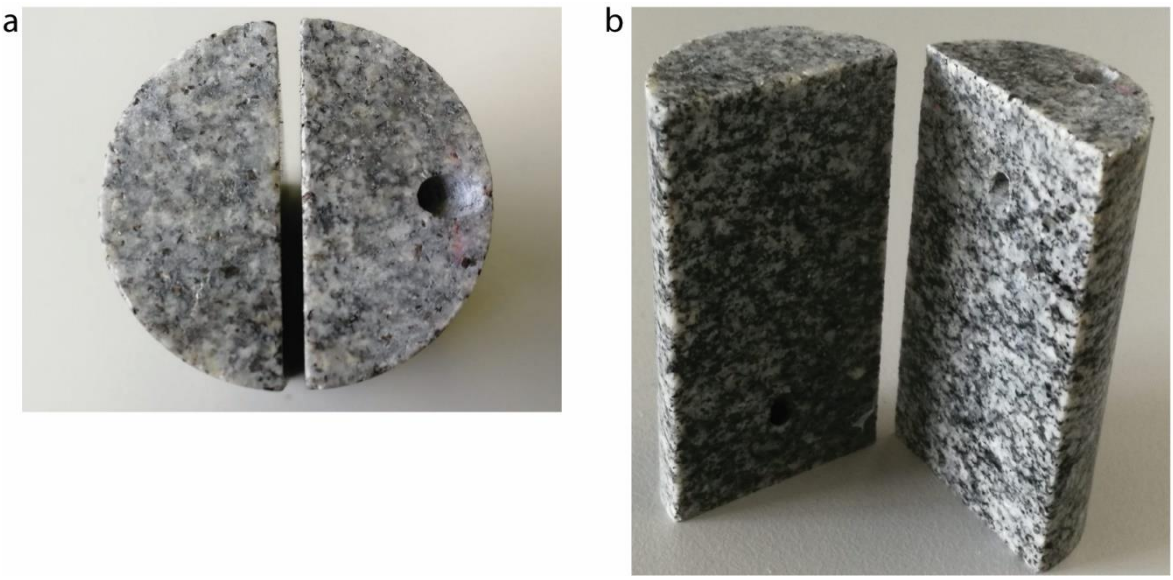

Figure 5 Samples for experiments performed in direct shear configuration in a triaxial deformation apparatus, (a) top view and (b) side view. On both half cylindrical samples, we drilled a borehole with inclination of 45° with respect to the both, the slip surfaces and the base of the semi-cylinder in order to allow the fluid to reach the fault surface.

Results

Our results showed that:

1. The fluid viscosity does not influence the static friction coefficient of the faults;
2. During slip:
    - An increase of slip velocity tends to stabilize the fault;
    - An increase of normal stress tends to destabilize the fault;

- And an increase of the viscosity of the pressurized fluid on the slip surface tends to destabilize the fault only in boundary lubrication regime.

This series of performed experiments shows that the increase of fluid viscosity promotes earthquakes nucleation at the laboratory scale. It is likely that similar mechanisms will be operative during hydraulic stimulation. While on the one hand an increased viscosity of the stimulation fluid promotes earthquake nucleation (stage II of the seismic cycle), on the other hand it may imped earthquake progatation for small slip earthquake (stage IV). Note that viscosity promotes fault weakening and earthquake propagation if the energy available is sufficiant to have large slip events.

2.4.3 STEP 3: Constant loading tests with viscous fluids

Experimental procedure

In order to complete the second objective of the project we adopted a new experimental approach consisting of a step-wise increase of shear stress on a pre-loaded fault (simulated with precut samples) which better simulates hydraulic stimulation in geothermal reservoir. Here, we reproduced the earthquake cycle in a laboratory fault under both room-humidity and drained pore fluid conditions (P_f=2 MPa).

Experiments were conducted in the rotary-shear machine SHIVA (Figure) on experimental faults in Westerly Granite saturated with fluids with increasing viscosity (at room temperature) over 4 orders of magnitude from 0.1 mPa.s (water) to 1.2 Pa.s (99% glycerol). Fault reactivation was triggered at constant effective normal-stress by increasing the shear stress acting on the fault (Figure 16). A comprehensive list and details on the experimental techniques can be found in Cornelio et al. (2020a) (see reference in paragraph 6).

Results

The evolution of shear stress and slip rate during the experiments can be described in terms of three stages (I, II, and III; Figure 6). Stage I: at each increment of shear stress, we observed a single pulse in slip-rate (Figure 6b). Stage II: with increasing shear stress, we observed spontaneous but isolated slip bursts events (Figure 6c). Stage III: For an applied shear stress higher than 6 MPa and, more in general, for a peak friction μ_{peak} =0.71±0.07, the frictional macroscopic behavior of the fault became unstable, showing tens of short-lived slip events (Figure 16d).

To understand the influence of fluid viscosity on the fault weakening mechanism active during stage III (especially during the last long-lived slip event), we analyzed the evolution of the apparent friction with slip and slip-rate. The analysis rests on a well-known weakening mechanism operative in the presence of fluids on a slip surface: flash heating, thermal pressurization and elasto-hydrodynamics. The experimental procedure, modeling, results and discussion for the experiments presented in this section have been published in Journal of Geophysical Research: Solid Earth (Cornelio et al., 2020a) (see reference in paragraph 6).

Conclusion

Our results showed that independent of the viscosity, fault reactivation followed a Coulomb-failure criterion. Instead, fluid viscosity affected the fault weakening mechanism: flash-heating was the

dominant weakening mechanism in room-humidity and water-saturated conditions, whereas the presence of more viscous fluids favored the activation of elasto-hydrodynamic lubrication (Figure 17). Independent of the weakening mechanism, the breakdown work W_b dissipated during seismic faulting increased with slip U following a power law ($W_b \propto U^{1.25}$) in agreement with seismological estimates of natural and induced earthquakes. Again, we interpret that such mechanisms will also be operative in the reactivation of faults in response to elevated pore pressures during hydraulic stimulation.

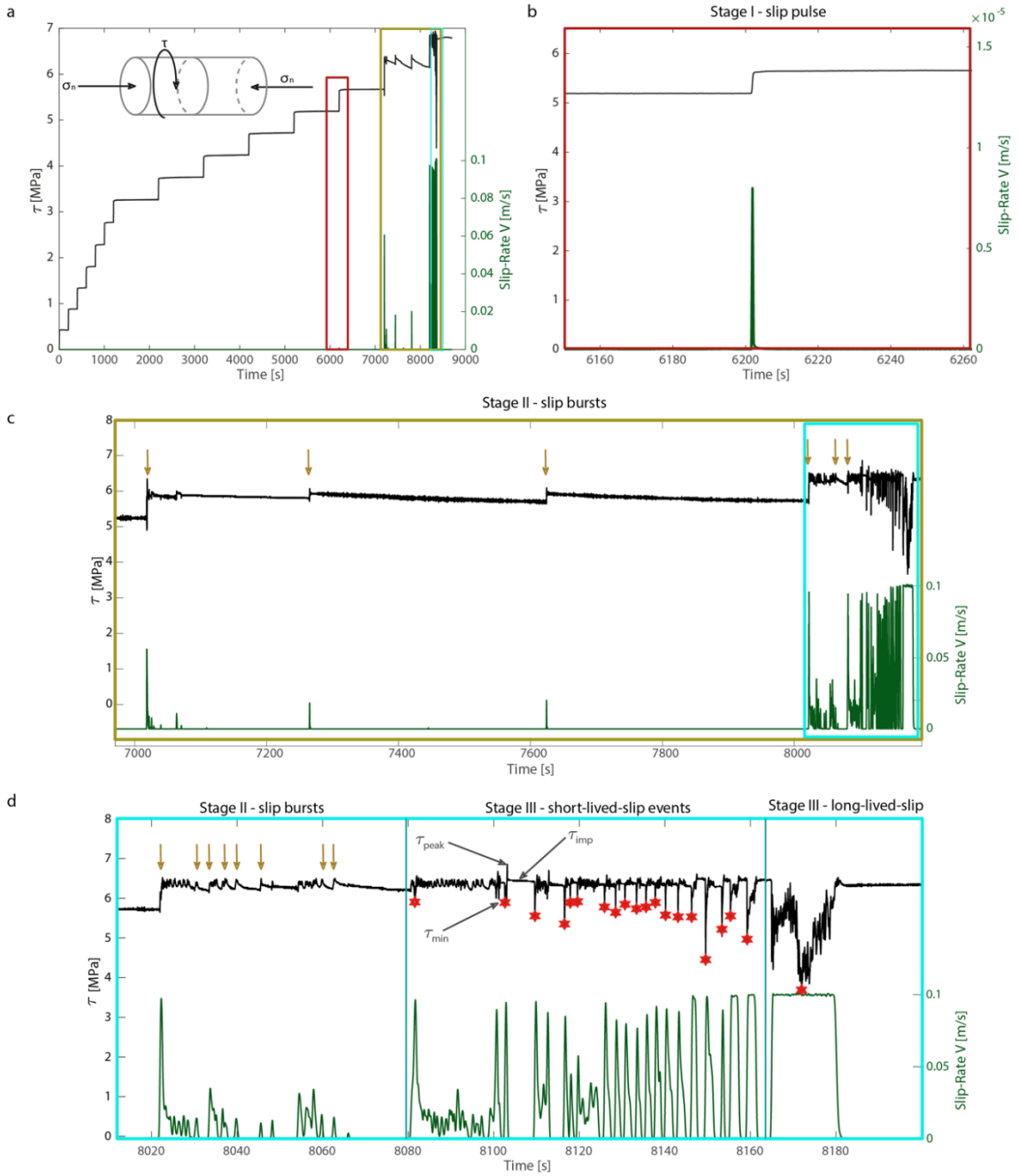

Figure 6: Experiment s1409 performed under ambient-humidity conditions. **a)** Shear stress τ and slip-rate V versus time. **b)** Zoom of the slip pulse associated to a shear stress perturbation during stage I. **c)** Zoom on the slip bursts (ocher arrows) during stage II. **d)** Zoom of the series of short-lived slip events

and single long-lived slip event corresponding to the stage III. The red stars indicated the minimum shear stress reached at each event τ_{min}. Figure from Cornelio et al. (2020a) (see reference in paragraph 6)

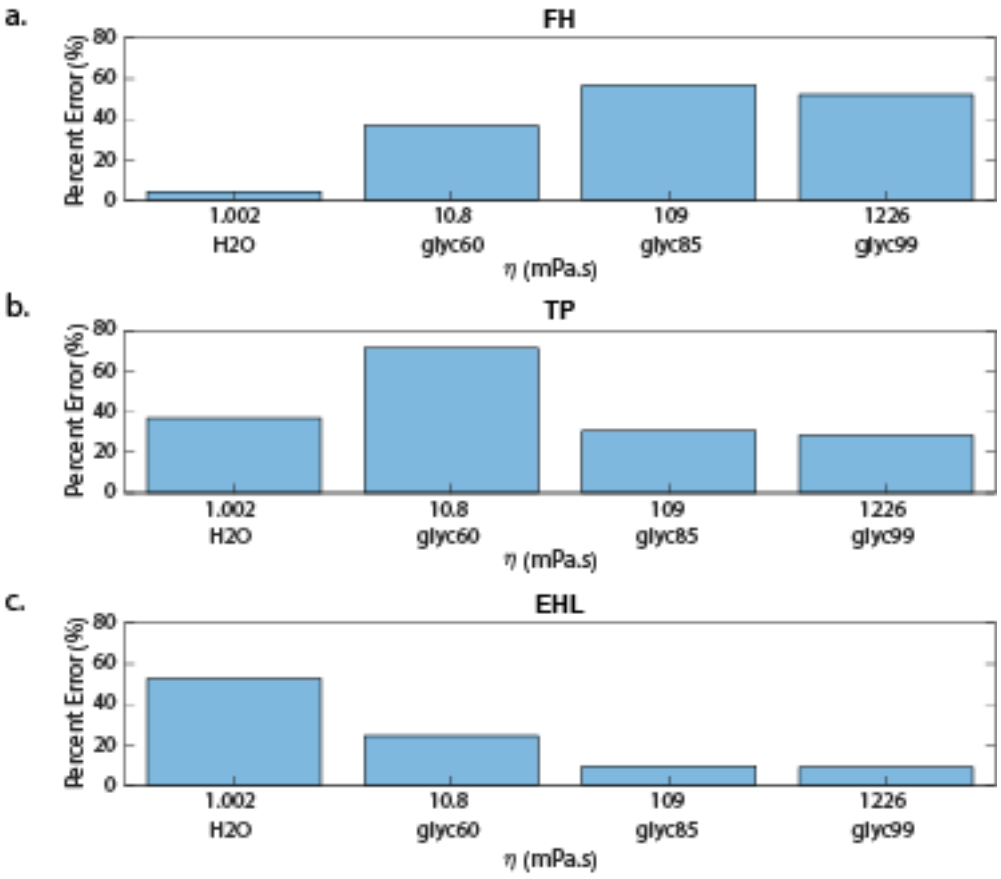

Figure 7: Misfit or percent error between the measured minimum shear stress and the estimated one for (a) Flash-Heating (FH), b) Thermal-Pressurization (TP) and c) Elastohydrodynamics (EHL) (see main text for discussion of Cornelio et al., 2020a) (see reference in paragraph 6). According to this analysis, FH **b)** Thermal-Pressurization (TP) and **c)** Elastohydrodynamics (EHL) (see main text for discussion of Cornelio et al., 2020a (see reference in paragraph 6)). According to this analysis, FH occurred only in the experiments performed with 100% distilled water, and EHL in the experiments performed with glycerol. Instead, modeling suggests that TP was never activated in the experiments. Figure from Cornelio et al. (2020a) (see reference in paragraph 6).

2.5 Summary of the performed experiments

Table 1: Summary of the performed experiments

	Rock lithologies & Sample type	P_{eff}	Condition	Viscosity	Temp	Slip-velocities	Shear stress	N. exp	Discussed key paramenters
STEP1									
Slip-velocities	Granite Saw cut	5 MPa 10 MPa 20 MPa	Room-humidity, fault saturated	Water, 60%glycerol 85%glycerol 99%glycerol	Room-Temperature, (the increase of temperature on the slip surface and its influence on fluid viscosity was estimated using a 2D heat diffusion model)	10 µm/s 100 µm/s 1mm/s 10 mm/s 1 cm/s 10 cm/s 1 m/s 5 m/s	measured	Performed: 60 Published: 40	Steady state fault friction, Fracture energy Critical slip distance Dc REF: Cornelio et al. (2019)
STEP 2									
Velocity steps exp	Granite Saw cut (new experimental procedure into triaxial apparatus)	30 MPa 50 MPa	Room-humidity, Fault saturated	Water, 60%glycerol 85%glycerol 99%glycerol	Room-Temperature	0.3µm/s 1 µm/s 3 µm/s 10 µm/s	measured	Performed: 50 (calibration of the new procedure) Published: 10	(a-b) parameters evolution with fluid viscosity REF: Cornelio

									and Violay (2020c)
STEP 3									
Stepwise increase of shear stress with constant normal stress and constant fluid pressure	Granite Saw cut	10 MPa	Room-humidity, Fault saturated	Water, 60%glycerol 85%glycerol 99%glycerol	Room-Temperature	Measured (up to max 0.1 m/s)	Step increase of 0.5 MPa	Performed: 15 Published: 10	Fault strength, efficiency of the weakening mechanism REF: Cornelio et al. (2020a)

2.6 Roughness measurements

It is highly likely and consistent with any constitutive relation that captures frictional behavior, that frictional behavior is highly influenced by the nature of the surfaces in contact and any fault gauge between those surfaces.

Before and after deformation, roughness measurements have therefore been performed on the majority of the samples to address the deformation mechanism affecting the behavior of the experimental fault. The roughness measurements have been performed using an optical profilometer Contour GT-I 3D Optical Microscope, Bruker Nano Surfaces Division. The measurements performed before the deformation guarantee a comparable initial state of the slip surface in terms of RMS (root mean square) deviation of the height of the asperities. The scan of the surfaces was performed imposing an overlap of 20% between two adjacent areas. For high velocities experiments series, RMS (root-mean-square) and the stitched images of the samples surface of Westerly Granite after the experiments performed under ambient humidity condition and in presence of the four different fluids at slip-rate of 1 m/s are shown in Figure . The RMS of the starting sample of Westerly Granite was around 13 µm.

Measurements performed after the deformation allowed us to define the RMS (Root mean square) of the samples and the regime they have reached (EHD, mixed lubrication and boundary regimes). The samples which slipped in the elasto-hydrodynamic regime have RMS values similar (same order of magnitude) to the initial intact slip surface, whereas the samples which slid into boundary or mixed lubrication regime have RMS values different (order of magnitude) from the initial value (gouges formation on the surface, melt formation on the surface). When the Sommerfeld number S was higher than 1 the RMS of the samples at the end of the experiments was of the same order of magnitude of the initial RMS.

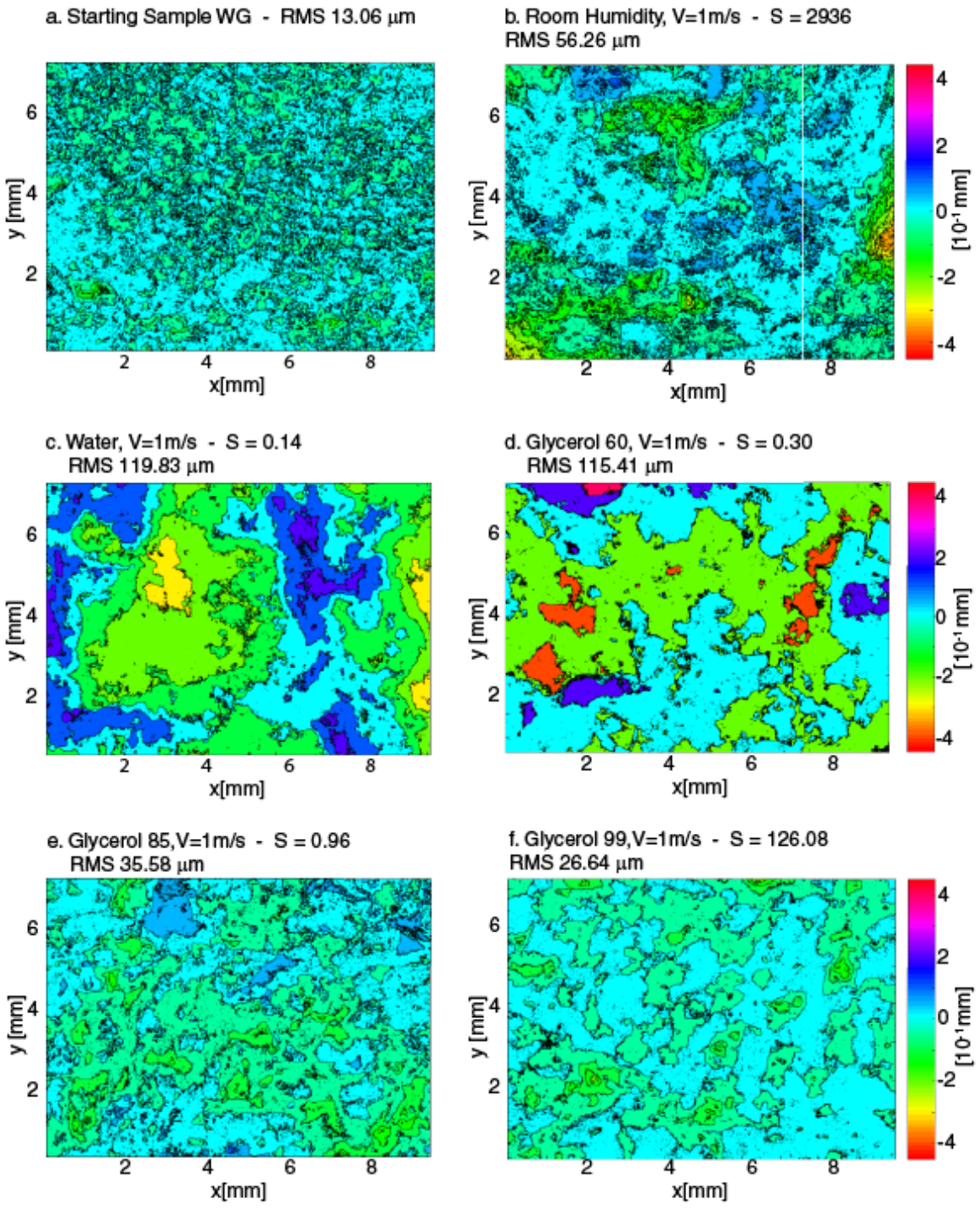

Figure 18: Examples of performed roughness measurements. Roughness of the sliding surfaces and RMS values in Westerly Granite. (a) Starting sample and sheared samples under (b) room-humidity conditions (exp s1321), (c) water (exp s1303), (d) 60%glyc/40%water (exp s1316), (e) 85%glyc/15%water (exp s1305), and (f) 99%glyc (exp s1389). All the experiments were performed at V = 1 m/s. Figure modified from Cornelio et al. (2019) (see reference in paragraph 6).

2.7 Parametric analysis of elasto-hydrodynamic lubrication efficiency on induced seismicity

Here, we perform a parametric analysis of the elasto-hydrodynamic fault lubrication mechanism to assess its efficiency during fluid-induced earthquakes, and hence by implication on hydraulic stimulation operations. The efficiency of the mechanism is measured with the nondimensional Sommerfeld number S.

Method

We analyze the possible range of minimum and maximum values for the parameters which defined the Sommerfeld number S (i.e. seismic velocity V, fault geometry parameters L and H, in situ state of stress acting on a possible fault P_{eff} and viscosities of the injected fluids η; see also Chapters 1 and 2.4.1). In that way, we can estimate the values of the expected Sommerfeld number for a specific fault geometry and injected fluid and thus infer whether or not boundary lubrication, mixed lubrication of elasto-hydrodynamic fault lubrication regimes has prevailed.

Moreover, we analyze eight well-documented cases of induced seismicity associated with the injection of fluids which viscosity ranges from 1 mPa.s (water) to 100 mPa.s (proppant-laden water). For each case, we collect the information related to the in-situ stress field, fault orientation and geometry, the moment of magnitude and static stress drop of the events (Table 2). These parameters allow us to analyze the variation of the Sommerfeld number.

Table 2 Summary of the case study reporting the magnitude, the viscosity of the injected fluid the average values of depth, effective stress P_{eff}, moment of magnitude M_0, stress drop ΔT slip of the event $\delta=L$ and asperity size of the fault.

Place	Mag	η	depth	σ_n	P_{eff}	M_0	Δτ	L	H
		[mPa s]	[km]	[MPa]	[MPa]	[1e14 Nm]	[MPa]	[m]	[mm]
Basel	3.4	1	4.7	97.95	88.45	1.60	6.81	0.16	0.31
Paradox Valley	4.3	10-30	4.2	79.75	32.49	31.60	10.00	0.14	0.18
Youngstown	3.9	10-30	3.7	77.40	46.86	12.30	11.83	0.08	0.19
Prague	5.6	30-50	4.5	79.17	38.67	3645.00	17.20	0.57	1.88
Timpson	4.7	30-50	3.5	64.85	29.21	221.00	23.06	0.48	1.93
Pawnee	5.7	30-50	5.5	93.50	93.50	4670.00	22.21	0.98	10.25
Fox Creek	3.9	100-200	3.5	85.90	21.79	61.22	27.25	0.13	0.19
Bowland Shale	2.3	100-200	3.6	73.73	18.73	0.03	15.88	0.01	0.01

Results and conclusions

Our results suggest that the estimated dynamic friction on the fault during the seismic event is compatible with fault elasto-hydrodynamic lubrication theory, particularly for cases where high viscous fluids have been used for injections (Figure).

However, at the moment, we can only estimate the values of the Sommerfeld number after the seismic event occurs and no statement can be provided before the event occurs.

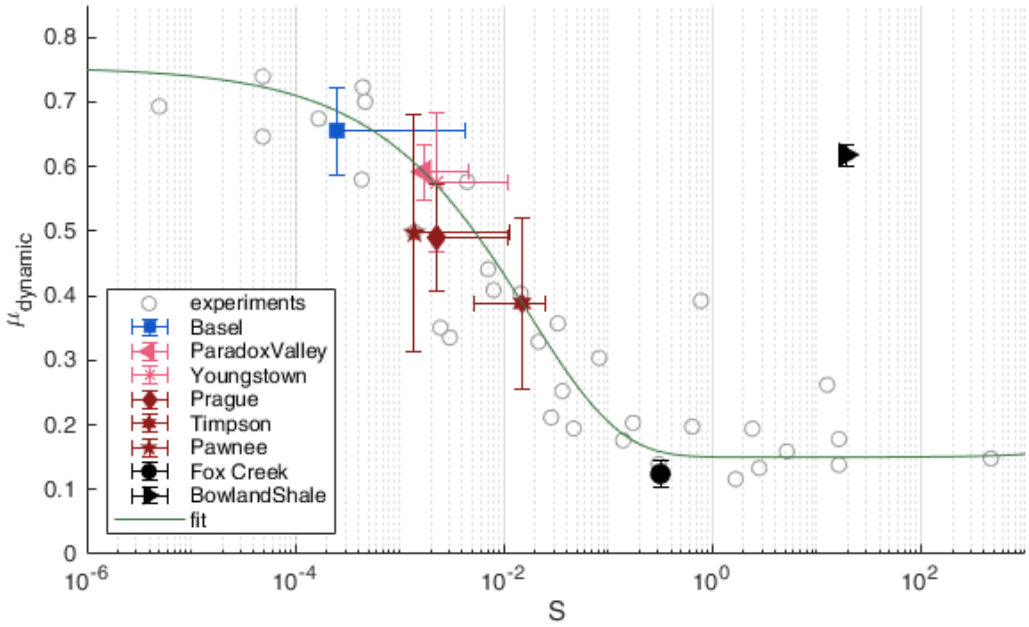

Figure 19 Estimated dynamic friction coefficient vs Sommerfeld number for induced seismicity cases. The grey empty circles are the experimental data of Cornelio et al. (2019) (see reference in paragraph 6), while the full marker are the estimated values of dynamic friction and Sommerfeld number for the case studied (see symbol in the figure). The three lubrication regimes (BL, ML, and EHD) are delimited by vertical black dashed lines. The dynamic friction coefficient μ_{dyn} in the three lubrication regimes decays from 0.75 in boundary lubrication regime to 0.1 at the boundary between the mixed and the hydrodynamic regimes. Figure modified from Cornelio and Violay (2020b) (see reference in paragraph 6).

3 Comments and recommendations

In the EDGAR project, we simulated via laboratory tests the fluid injection into geothermal reservoir crossed by faults at different state of stability. We attempted to identify the physical parameters that control fracturing and fracture reactivation (i.e. stress state, fracture geometry, leak of rate, fluid rheology, rock mass properties). The final fracture shape during hydraulic stimulations, size, and conductivity can be predicted only through a good understanding of the influence of each of these parameters on rupture propagation. Because proppants or constituents comprising green or environmentally friendly stimulation fluids can be added during reservoir stimulation to enhance fracture propagation, limit leak off and enhance permeability, we focused on the effect of fluid viscosity on fault mechanical behavior.

Experiments were performed on granite because this rock type will be representative of EGS host rocks in Switzerland. In a first step, we imposed a series of computer-controlled changes in sliding velocity on precut sample, mimicking fault saturated behavior. In a second step, we adopted a new experimental procedure consisting of a stepwise increase of shear stress on a preloaded saturated fault, which better simulated change in stress distribution in geothermal reservoir. Finally, we expressed the data via theoretical frictional models. This allowed quantitatively linking and re-scaling the results to natural induced seismicity.

At present the results of the project allows mostly general considerations about fault reactivation (i.e. the achievement of critical unstable frictional behavior of the fault) and co-seismic slip propagation in geothermal reservoirs. The analyses show that:

1) Independent of the viscosity, fault reactivation (which happens when the static friction coefficient is overcome) followed Mohr-Coulomb friction criterion. However, the static fault strength decreases with the viscosity of the fluid. The presence of high viscosity fluid is then expected to promote the onset of slip along fault.

2) During the laboratory simulation of co-seismic slip, the fault weakening mechanisms depend on fluid viscosity. In particular, high viscosity of fluid on faults promotes elastohydrodynamic lubrication. This lubrication mechanism is governed by the Sommerfeld number S, defined as $S=\eta VL/P_{eff}H^2$ where η is the fluid viscosity at the mean estimated surface temperature at steady state, V is the slip-rate, P_{eff} is the effective normal stress, L is the characteristic slip length and H is the initial average asperities height. Particular combinations of fault geometry (L/H^2), fluid viscosity, fault depth (proportional to the effective normal stress acting on the fault P_{eff}) can lead the fault into the fully lubricated regime. This regime of lubrication of the fault is associated to low value of dynamic friction coefficient, and longer slip necessary to stop the slip propagation.

3) However, if the fully lubricated regime is not reached by the fault, a high value of fluid viscosity increases the fracture energy and the slip necessary to propagate the rupture. Using the energy balance to extrapolate these results from the laboratory experiments to the man-induced seismicity we can assume that an increase of fluid viscosity on the fault can favor slow-slip rather than rupture propagation for small to moderate earthquakes, but increase the intensity for large earthquakes.

It is important to keep in mind that high fluid viscosity strongly limits fracture leak off (enhancing the efficiency of hydro-fracturing mechanism) and reduces diffusion rate in fault zone, thus reducing the area over-pressurized by fluids. The area over-pressurized by fluid has an important influence on the probability of earthquake occurrence as observed by (Shapiro and Sinske, 2009). This reduction of the diffusion length (because of the high viscosity of the fluid) is expected to reduce the rupture length, i.e. the size and the intensity of the induced seismicity.

However, our work also highlights that fluid viscosity is also a critical parameter for the control of slip dynamics in experimental faults and we suggest that a similar behavior can be expected in case of man-induced seismicity. In particular, conditions of fault geometry and surrounding stresses of the fault, high fluid viscosity might favor larger earthquakes if the system and the reservoir are saturated with viscous fluid. Moreover, it can be important to collect fault gauge and fault rock samples during first phases of characterization of a geothermal project, i.e. before fluid stimulations. Indeed, Faults roughness characterization can condition the viscosity of the stimulation fluid.

Our experimental results are consistent with stress drops observed during human induced events being larger values than natural earthquakes.

4 National and international Cooperation

Passelègue F., LEMR Ecole Polytechnique Fédérale de Lausanne, Lausanne, Switzerland. (knowledge transfer)

Spagnuolo E. Istituto Nazionale di Geofisica e Vulcanologia, Rome, Italy (laboratory test)

Di Toro G. Università degli studi di Padova, Padua, Italy (laboratory test)

Nielsen S. Durham University, Durham, United Kingdom (knowledge transfer)

5 Communication

TALKS

- C. Cornelio; E. Spagnuolo; F. Passelègue; S. Neilsen; G. Di Toro; M. Violay : **Earthquake reactivation and propagation in presence of viscous fluids**; AGU 2019, San Francisco, USA, December, 9-13, 2019.
- C. Cornelio; F. Passelègue; E. Spagnuolo; G. Di Toro; M. Violay : **Earthquake nucleation in presence of viscous fluids: Thermal Pressurization or Elastohydrodynamic Lubrication?** ; EGU 2019, Vienna, Austria, April, 7-12, 2019.
- C. Cornelio; E. Spagnuolo; F. Passelègue; S. Nielsen; G. Di Toro; M. Violay: **Mechanical behaviour of fluid-lubricated faults;** GeoMod 2018, Barcellona, October, 1-4, 2018
- C. Cornelio; E. Spagnuolo; G. Di Toro; M. Violay : **Fluid viscosity controls earthquakes nucleation** ; SEG 2018, Lausanne, Switzerland, September 25-28, 2018.
- C. Cornelio; E. Spagnuolo; G. Di Toro; M. Violay : **Fluid viscosity controls earthquakes nucleation** ; EGU 2018, Vienna, Austria, April 9-13, 2018.
- C. Cornelio; M. Violay; E. Spagnuolo; G. Di Toro : **Effect of fluid viscosity on fault frictional behaviour** ; EGU 2017, Vienna, Austria, April, 23-28, 2017.

POSTERS

- M. Violay; C. Giorgetti; C. Cornelio; G. Di Stefano; S. Weimer; J.-P. Burg : **A New State-of-art Apparatus to Study Earthquake Nucleation and Propagation: HighSTEPS** ; EGU 2019, Vienna, Austria, April, 7-12, 2019.
- M. Violay; C. Giorgetti; C. Cornelio; G. Di Stefano; S. Weimer; J.-P. Burg : **A New State-of-art Apparatus to Study Earthquake Nucleation and Propagation: HighSTEPS** ; AGU 2018, Washigton D.C., USA, December, 10-14, 2018.
- M. Violay; C. Giorgetti; C. Cornelio; G. Di Stefano; S. Weimer; J.-P. Burg : **A New State-of-art Apparatus to Study Earthquake Nucleation and Propagation: HighSTEPS** ; 16th Swiss Geosciences Meeting, Bern, Switzerland, December, 1, 2018.

- C. Cornelio; F.X. Passelègue; E. Spagnuolo; G. Di Toro; M. Violay : **Role of fluid viscosity in earthquakes nucleation** ; Geoproc2019: Earthquakes and faulting mechanisms, Utrecht, Netherlands, July, 3-5, 2019

- C. Cornelio; E. Spagnuolo; G. Di Toro; M. Violay : **Effect of fluid viscosity on granitic fault frictional behavior** ; EARTHQUAKES: nucleation, triggering, rupture, and relationships to aseismic processes, Cargese, France.

- C. Cornelio; E. Spagnuolo; G. Di Toro; M. Violay : **Effect of fluid viscosity on fault frictional behaviour** ; SCCER-SoE Annual Conference 2017, Birmensdorf, Switzerland, September, 14-15, 2017

- C. Cornelio; M. Violay; E. Spagnuolo : **Viscosity fluid influence on stick-slip motions**; 14 th Swiss Geoscience Meeting, Geneva, Switzerland, Novemeber, 18-19, 2016

6 Publications

C. Cornelio, E. Spagnuolo, G. Di Toro, S. Neilsen, and M. Violay (2019), **Mechanical behavior of fluid-lubricated faults**, Nature Communications, 10, 1274, doi:10.1038/s41467-019-09293-9

C. Cornelio, F.X. Passelègue, E. Spagnuolo, G. Di Toro, and M. Violay (2020a)**, Effect of fluid viscosity on fault reactivation and co-seismic weakening**, Journal of Geophysical Research - Solid Earth, 125, e2019JB018883, doi:10.1029/2019JB018883.

C. Cornelio, and M. Violay (2020b), **Parametric analysis of the elastohydrodynamic lubrication efficiency on induced seismicity**, Geophysical Journal International, 222 (1), 517–525, doi:10.1093/gji/ggaa180.

Cornelio, C., and Violay, M. (2020c), **Effect of Fluid Viscosity on Earthquake Nucleation. Geophysical Research Letters**, 47, e2020GL087854. doi:10.1029/2020GL087854.